SYNTHESIS AND OPTICAL PROPERTY OF TITANIA NANOTUBES FOR SOLAR CELLS

EMMANUEL NYAMBOD TIMAH

A THESIS SUBMITTED IN PARTIAL FULFILLMENT OF THE
REQUIREMENTS FOR THE DEGREE OF DOCTOR OF PHILOSOPHY
MAJOR IN PHYSICS
FACULTY OF SCIENCE
UBON RATCHATHANI UNIVERSITY
ACADEMIC YEAR 2015

UBON RATCHATHANI UNIVERSITY
THESIS APPROVAL
DOCTOR OF PHILOSOPHY
IN PHYSICS FACULTY OF SCIENCE

TITLE SYNTHESIS AND OPTICAL PROPERTY OF TITANIA NANOTUBES FOR SOLAR CELLS

AUTHOR MR. EMMANUEL NYAMBOD TIMAH

EXAMINATION COMMITTEE

ASSOC. PROF. DR. TOSAWAT SEETAWAN	CHAIRPERSON
ASST. PROF. DR. UDOM TIPPARACH	MEMBER
DR. CHRISTIAN HERBST	MEMBER

ADVISOR ……………………………………………

(ASST. PROF. DR. UDOM TIPPARACH)

……………………………………………
(ASSOC. PROF. DR. UTITH INPRASIT)
DEAN, FACULTY OF SCIENCE

……………………………………………
(ASSOC. PROF. DR. ARIYAPORN PONGRAT)
VICE PRESIDENT
FOR ACADEMIC AFFAIRS

ACADEMIC YEAR 2015

ACKNOWLEDGEMENT

I am very grateful to all whom in one way or another contributed to the accomplishment of this thesis. Special thanks go to my supervisor, Asst. Prof. Dr. Udom Tipparach, who was more like a father to me. Thanks to the thesis committee members for their vital comments and suggestions. I'm thankful to all the thesis committee members – Assoc. Prof. Dr. Tosawat Seetawan, Asst. Prof. Dr. Udom Tipparach and Dr. Christian Herbst, for their technical and intellectual advice.

I'm glad to express my sincere gratitude to the following persons: Asst. Prof. Dr. Tanin Nataro (for his advice), Mrs. June Tipparach (for her advice), Mr. Wichean Piwbang and Narongsak Nodtharin (for XRD data), Miss Thairoh Saenwang (for SEM images), Miss Pisichana Sisuan (for UVS data), Miss Nuan La-ongSrakaew (for EDX data), Mrs. Rinnatha Vongwantthaporn (for XPS data), Dr. Buagun Samran (DSSC), Mr. Saichon (for anodization apparatus).

Furthermore, I thank the staff of the Department of Physics and Registration Office, of Faculty of Science, Ubon Ratchathani University for their technical supports. Finally, I thank my mother (Mrs. Julie Atud), my late father (Mr. Timah David), my brothers (Timah John Mbahgwe and Ndi Emmanuel), my sisters (Solange Timah and Mar Rosaline Timah), my aunt (Mrs. Fontem Magdaline), uncle (Mr. Njei Emmanuel and family), and all others who gave their support and encouragement towards the completion of this research work. Thank you so much.

Emmanuel Nyambod Timah
Researcher

DEDICATION

I dedicate this thesis to the Almighty God. And to His begotten Son Jesus Christ, who through His finished work on the cross has brought unto mankind salvation (- eternal life, forgiveness of sins, healing from every sickness, wisdom beyond human understanding, freedom from oppression, prosperity and success, and the ever comforting presence of His Holy Spirit).

To God be the Glory!!!

บทคัดย่อ

เรื่อง : การสังเคราะห์และสมบัติทางแสงของท่อนาโนไททาเนียมสำหรับเซลล์แสงอาทิตย์
ผู้วิจัย : EMMANUEL NYAMBOD TIMAH
ชื่อปริญญา : ปรัชญาดุษฎีบัณฑิต
สาขาวิชา : ฟิสิกส์
อาจารย์ที่ปรึกษา : ผู้ช่วยศาสตราจารย์ ดร.อุดม ทิพราช
คำสำคัญ : TiO_2 ท่อนาโนไนโตรเจน, การโด้ป, เซลล์แสงอาทิตย์สีย้อมไวแสง, การแอโหนดไดเซชัน, แถบช่องว่างพลังงาน

ท่อนาโนไททาเนียได้ถูกสังเคราะห์โดยวิธีดีซีแอโหนดไดเซชันในสารละลายอิเล็กโทรไลต์เอธิลีนไกลโคล แอมโมเนียมฟลูออไรด์ และน้ำปราศจากไดออน ท่อนาโนไททาเนีย 2 ชุดได้ถูกเตรียมขึ้นโดยการโด้ปไนโตรเจน ในชุดที่ 1 ปริมาณของแอมโมเนียถูกเติมโดยแปรค่าในปริมาณต่าง ๆ ในขณะที่ชุดที่ 2 อุณหภูมิของการบำบัดถูกแปรเปลี่ยน ตัวอย่างที่ได้ถูกวิเคราะห์เชิงพื้นผิวด้วยกล้องจุลทรรศน์อิเล็กตรอนแบบส่องกราด วิเคราะห์โครงสร้างทางจุลภาคด้วยเทคนิคการเลี้ยวเบนรังสีเอกซ์ วิเคราะห์สมบัติทางแสงโดยเทคนิคยูวีวิซิเบิลสเปกโตรสโคปีวิเคราะห์องค์ประกอบทางเคมีของพื้นผิวด้วยเทคนิคการกระจายพลังงานของรังสีเอกซ์และเอกซ์เรย์โฟโตอิเล็กตรอน การทำงานของแต่ละตัวอย่างถูกทดสอบในการทำเป็นเซลล์แสงอาทิตย์สีย้อมไวแสงได้ประสบความสำเร็จในการลดแถบช่องว่างพลังงานลงจาก 3.15 อิเล็กตรอนโวลต์ ไปสู่ 2.99 อิเล็กตรอนโวลต์สำหรับทั้งสองชุด แถบพลังงานที่ 2.85 อิเล็กตรอนโวลต์ สมนัยกับการเลื่อนไปทางความยาวคลื่นสีแดงของการดูดกลืน 435 นาโนเมตร ในชุดที่ 1 เซลล์แสงอาทิตย์สีย้อมไวแสงมีประสิทธิภาพสูงสุด 7.89% เมื่อเติมแอมโมเนีย 6% โดยปริมาตร ในขณะชุดที่ 2 เซลล์แสงอาทิตย์สีย้อมไวแสงมีประสิทธิภาพสูงสุด 4.62 % เมื่อบำบัดร้อนที่ 125 องศาเซลเซียส ค่านี้คิดเป็นเพิ่มขึ้นร้อยละ 50 และร้อยละ 42 สำหรับชุดที่ 1 และ 2 ตามลำดับ

ABSTRACT

TITLE : SYNTHESIS AND OPTICAL PROPERTY OF TITANIA NANOTUBES FOR SOLAR CELLS
AUTHOR : EMMANUEL NYAMBOD TIMAH
DEGREE : DOCTOR OF PHILOSOPHY
MAJOR : PHYSICS
ADVISOR : ASST. PROF. UDOM TIPPARACH, Ph.D.
KEYWORDS : TiO_2 NANOTUBES NITROGEN, DOPING, DYE-SENSITIZED SOLAR CELLS, ANODIZATION, OPTICAL BAND GAP

Nanotubes of TiO_2 were synthesized by DC Anodization in an electrolyte solution of ethylene glycol (EG), ammonium fluoride (0.3 % wt NH_4F) and deionized water (2 % vol H_2O). Two sets of N-doped TiO_2 nanotubes were prepared using ammonia (NH_3) as Nitrogen source. In Set 1, the amount of ammonia was varied while in Set 2, the calcination temperature was changed. The samples were analyzed using Scanning Electron Microscope (SEM), X-ray diffraction (XRD), UV-Visible Spectrometry (UVS), Energy dispersive X-ray Spectroscopy (EDX), and X-ray Photoelectron Spectroscopy (XPS). The performance of each sample was tested in adye-sensitized solar cell (DSSC).

In both sets, the optical band gap was successfully reduced from 3.15 eV to 2.85 eV in Set 1, and from 3.46 eV to 2.99 eV in Set 2.A band gap of 2.85 eV corresponds to a red shift in light absorption into the visible region with wavelength of 435 nm. XPS results confirm the successful doping of the samples with Nitrogen in both Sets 1 and 2. Overall, Set 1 samples performed better in the DSSC than Set 2 samples. The maximum power conversion efficiency (η) of DSSCsin Set 1 was 7.89 %, obtained for the sample doped with 6 % vol NH_3. A lower $\eta$of 4.62 % was obtained for the sample calcinated at 125°C in Set 2. The efficiencies 7.89 % and 4.62 % respectively correspond to approximately 50 % efficiency improvement in Set 1 and 42 % in Set 2.

CONTENT

CONTENT (CONTINUED)

PAGE

CHAPTER 5 CONCLUSION AND RECOMMENDATIONS

LIST OF TABLES

LIST OF FIGURES

FIGURE **PAGE**

LIST OF FIGURES (CONTINUED)

LIST OF FIGURES (CONTINUED)

LIST OF APPREVIATIONS

DSSC	Dye-sensitized solar cell
Ti	Titanium
TiO_2	Titanium dioxide or titania
Pt	Platinum
TNT	TiO_2 nanotube
N-TNT	Nitrogen-doped TiO_2 nanotube
SEM	Scanning Electron Microscope
XRD	X-ray diffraction
UVS	UV-Visible Spectrometry
EDX	Energy dispersive X-ray Spectroscopy
XPS	X-ray Photoelectron Spectroscopy
IV curve	current – voltage curve
NH_3	ammonia
EG	ethylene glycol
NH_4F	Ammonium fluoride
D.I. H_2O	Deionized water
DC	Direct current
AM	Air mass
TCOG	transparent conducting oxide glass
FTO	Fluorine-doped tin oxide
Ru	Ruthenium
I_3^-/I^-	tri- iodide/ iodide
HOMO	Highest occupied molecular orbital
LUMO	Lowest unoccupied molecular orbital
CB	Conduction band
VB	Valence band
D/ D^*	Ground state/excited state of dye molecule
D^+	Oxidized state of dye molecule
IPCE	incident photon-to-current conversion efficiency

LIST OF APPREVIATIONS (CONTINUED)

LHE	light harvesting efficiency
η	solar energy-to-electricity conversion efficiency
P_M	maximum output power
I_M	current at maximum output power
V_M	voltage at maximum output power
P_{in}	power of the incident light
V_m	Wavelength of incident radiation
I_{SC}	short-circuit current density
V_{OC}	open-circuit voltage
FF	fill factor
$\mathbf{E_g}$	band gap energy
ε	semiconductor electric permittivity
$\mathbf{e}$	electronic charge
q	charge
n_o	equilibrium electron concentration
p_o	equilibrium hole concentration
N_D^+	ionized donor concentration
N_A^-	ionized acceptor concentration
E_F	Fermi energy
T	Kelvin temperature
k	Boltzmann's constant
γ	Shape factor or Scherrer constant
E_D	donor energy of state
E_A	acceptor energy of state
g_D	donor and acceptor degeneracy factors
g_A	donor and acceptor degeneracy factors
E_C	Lowest Energy level at bottom of the conduction band
E_V	highest Energy level at top of the valence band
$\vec{E}$	electric potential

LIST OF APPREVIATIONS (CONTINUED)

φ	electric field
Å	Armstrong (10^{-10}m)
DBGS	direct band gap semiconductors
IBGS	indirect band gap semiconductors
$\boldsymbol{\alpha_a}$	absorption coefficient $\boldsymbol{\alpha_a}$
$\boldsymbol{\alpha}_{\mathrm{e}}$	emission coefficient $\boldsymbol{\alpha}_{\mathrm{e}}$
NHE	Normal hydrogen electrode
f	Frequency of incident photon
h	Planck's constants ($\hbar = h/2\pi$)
SLT	single level trap
υ_{th}	thermal velocity υ_{th}
N_T	concentration of traps N_T
σ	capture cross section σ
τ_{SLT}	Single level trap carrier lifetime τ_{SLT}
τ_λ	lifetime τ_λ
R_{SLT}	single level trap recombination rate
R_λ	radiative recombination rate
R_A	Auger recombination rate
Q_{sca}	scattering coefficient
Q_{ext}	extinction coefficient
r	Radius of nanoparticle
ZnSe	Zinc selenide
QD	Quantum dot
MHz	Mega hertz
GHz	Giga hertz
1 D	One dimension
Ψ	Wave function
λ	Wavelength
D	Crystallite size
d	Distance between crystal planes

LIST OF APPREVIATIONS (CONTINUED)

β	Full width at half maximum
(hkl)	Miller indices
E_B	Binding energy

CHAPTER 1
INTRODUCTION

This research work is entitled "*Synthesis and Optical Properties of Titanium dioxide Nanotubes for Solar Cells*". In this chapter, the rationale of this work, previous reports and ongoing research on Titanium dioxide for photovoltaic and energy conversion devices are presented.

1.1 RATIONALE

The global energy crisis such as pollution due to emission of green-house gases, energy shortage due to growing population and expanding industrialization, and exhaustion of natural energy sources such as fossil fuels, coal, oil and natural gas, has triggered the need for developing alternative sources of energy that are renewable, clean and low cost.

Solar energy is an excellent energy source because it is natural, abundant and inexhaustible. Solar cells and other photovoltaic devices are being used to harness energy from the sun. The invention of the dye-sensitized solar cells (DSSCs) by Gratzel and O'Regan in 1991 [1] has led to intensive research to improve solar cell efficiency.

TiO_2 as a semiconductor has been extensively studied in recent years due to its high photocatalytic activity, dielectric effect, resistance to corrosion, nontoxicity, and low cost. These unique properties make it a suitable material for several applications such as in photocatalysis [1], humidity sensing [2], water splitting [3], hydrogen generation [4], and gas sensing [5].

The use of TiO_2 means its solar energy absorption is restricted mostly in the ultraviolet region due to its large energy band gap (3.2 eV for anatase). In addition, a high rate of charge recombination limits its practical applications. These problems can be solved by modifying the structure of titania through doping with foreign ions [6, 7] or through developing nanotubes of TiO_2 [8, 9].

TiO_2 nanotubes have been successfully fabricated using techniques such as hydrothermal [10], solvothermal [11], sol-gel [12] and anodization [13-15] methods. Of these methods, anodization is a more suitable method due to its simplicity and low cost. Several parameters have been investigated in the preparation and application of titania nanotubes. These include: electrolyte composition, electrolyte pH, anodization time, anodizing voltage, dopant element and annealing temperature [16 -21].

Xiaobo Chen et al (2007) reported effects of electrolyte composition and applied voltage on TNTs [22]. Hao Xu and et al (2011) presented the influence of ultrasonic cleaning on TNT structure [23]. Wanichaya Mekprasat and Wisanu Pecharapa [24] in 2011 reported enhanced photocatalytic activity of N-doped titania nanopowders by adjusting annealing time at 100 °C and changing the N concentrations.

Zuoli He, Wenxiu Que, et al [25] in 2013 reported on the photocatalytic performance of Nitrogen-doped TiO_2 nanotubes arrays powders prepared by combining anodization with solvothermal process. By varying the treatment temperature, they obtained an optimal result for the sample after solvothermal treatment at 100 °C for 3 hours. The anodization voltage was kept constant at 50 V using a DC power supply for 6 hours.

Narongsak Kodtharin, Rinnatha Vongwatthaporn and Udom Tipparach in 2014 reported the effect of annealing temperature on the phase transformation of TNTs [18]; Emmanuel Timah, Buagun Samran and Udom Tipparach in 2014 demonstrated the dependence of TNTs morphology on anodization time [19]. In all these papers, there is not sufficient report on how calcination temperature and dopant amount affect the optical properties. Especially, when doping with Nitrogen, using ammonia as source of the doping element. In this paper we intend to modify the structure of TiO_2, and investigate the effects of calcination temperature and dopant concentration on its optical properties. We will analyze the samples by SEM, XRD, UVS, EDX and XPS. The performance of the samples will be tested in DSSCs.

1.2 OBJECTIVES

1.2.1 To modify structure of titania by synthesizing nanotubes anddoping with foreign ions such as Nitrogen.

1.2.2 To study the optical properties of titania by SEM, XRD, UVS, EDX and XPS characterizations, and performance test in solar cells.

1.3 SCOPE OF RESEARCH

The TiO_2 nanotubes will be produced by DC Anodization in an electrolyte composed of ethylene glycol (EG), ammonium fluoride (0.3 wt % NH_4F) and deionized water (2 vol % H_2O). The optical properties of TiO_2 nanotubes will be improved through structural modification by doping with Nitrogen using ammonia (NH_3) as source. The samples will be analyzed using the following techniques: Scanning Electron Microscope (SEM) to investigate the surface morphology and microstructure; X-ray diffraction (XRD) to determine the crystal structure;UV-Visible Spectrometry (UVS) to analyze the absorbance and optical band gap, Energy dispersive X-ray Spectroscopy to study the elements present on the sample surface and X-ray Photoelectron Spectroscopy (XPS) to determine the chemical composition of the TNTs through their binding energies. Finally, the performance of each sample will be tested in dye-sensitized solar cells. The current – voltage (IV) curve will be plotted to determine the efficiencies of the cells. The scope of this work is summarized in Figure 1.1

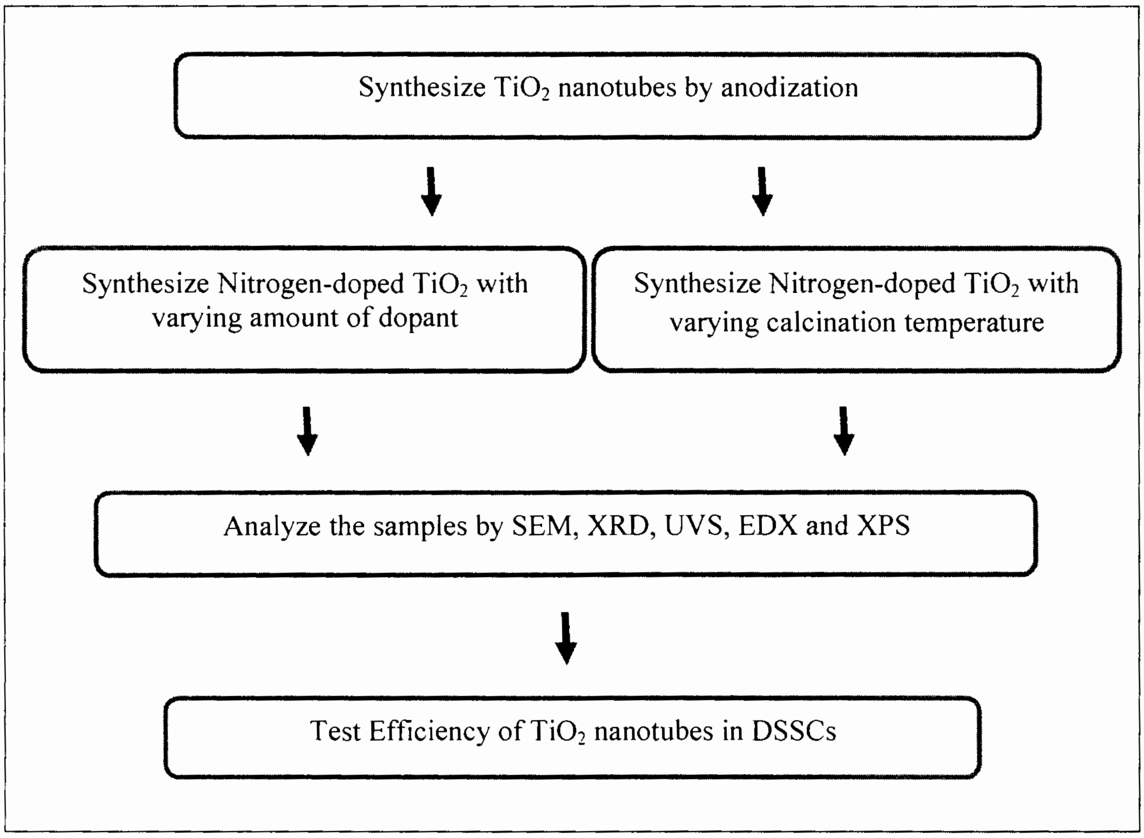

Figure 1.1 Flow chart summarizing the scope of this research

CHAPTER 2

THEORETICAL AND LITERATURE REVIEW

This chapter covers theoretical review and some fundamental information about the solar spectrum, photovoltaic cells, semiconductor electronic structure, properties of Titanium dioxide, structural modification of TiO_2 through developing nanotubes and doping with Nitrogen, and the mechanism of formation of TiO_2 nanotubes by DC Anodization.

2.1 SOLAR SPECTRUM AND AIR MASS

The radiation spectrum of the sun can be approximated to that of a black body at 6000 K, as shown in Figure 2.1. The solar spectrum on Earth is attributed to photons emitted directly towards the Earth. The radiation intensity just above the Earth's atmosphere is about 1.353 kW/m^2. This value is called the solar constant [26], and corresponds to the air mass zero (AM0) radiation spectrum. The Air Mass number is used to quantify the effects of atmospheric absorption on solar radiation intensity and spectral content. Figure 2.2 shows that Air Mass varies with zenith angle θ, and can be calculated using the following equation

$$Air\ Mass = \frac{1}{cos\theta} \tag{2.1}$$

Air Mass can also be determined using the length L and height H of an object's shadow, according to the following equation by Green [27]

$$Air\ Mass = \sqrt{1 + \left(\frac{L}{H}\right)^2} \tag{2.2}$$

The performance of solar cells are usually compared using the AM 1.5 spectrum normalized to an intensity of 1 kW/m^2.

2.2 PHOTOVOLTAIC CELLS

Solar cells

Photovoltaic devices convert solar energy into electricity. The basic component of a photovoltaic system is a solar cell. Solar cells can be arrayed to form a solar panel. Figure 2.3 shows a simple diagram of a solar panel. A solar cell operates as a semiconducting device. When light falls on a solar cell, an electron in the valence band absorbs a photon of appropriate energy and jumps into the conduction band. This leaves a vacancy or hole, which can be filled by another neighboring electron. This electron also leaves another hole behind as it moves in to fill the hole. Thus, an electron-hole pair is created whose mobility generates an electric current.

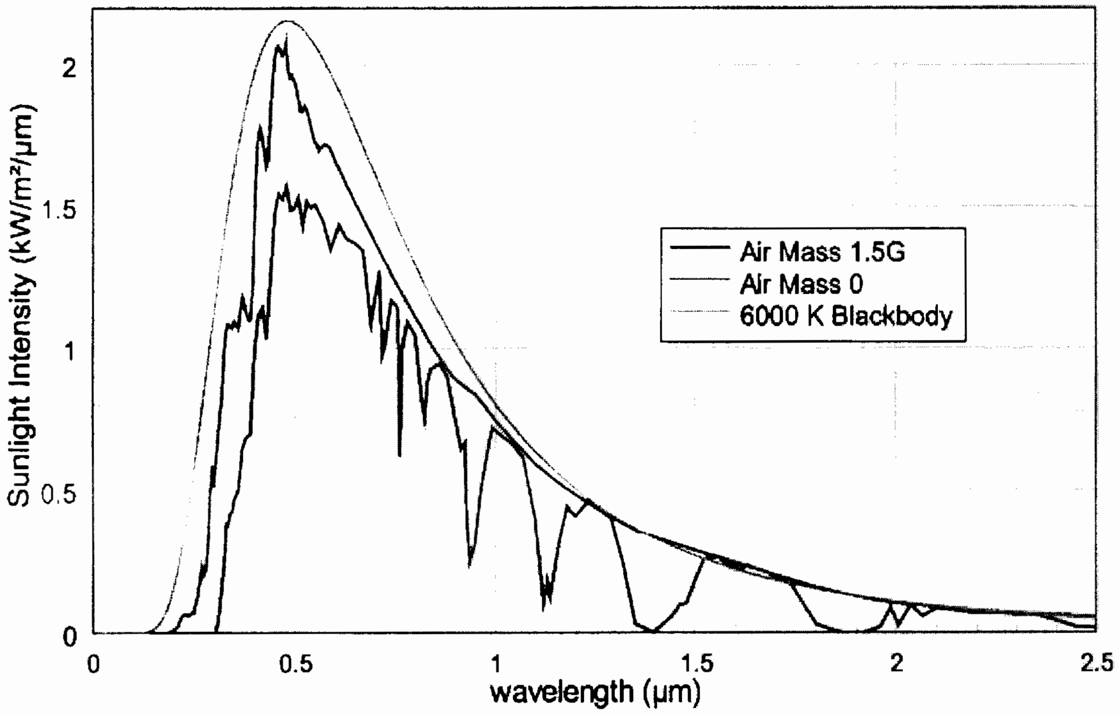

Figure 2.1 AM 0 and AM 1.5 spectra compared to a black body at 6000 K [26]

Solar cells can be classified into first, second and third generations. First generation solar cells are made of silicon wafers, second generation solar cells are made of thin film semiconductor materials, while dye-sensitized solar cells, organic or polymer cells are good examples of third generation solar cells. Multi-junction solar cells have also been developed by combining different semiconducting materials together. Such cells are called tandem cells. Table 2.1 shows the maximum reported efficiency of different types of solar cells.

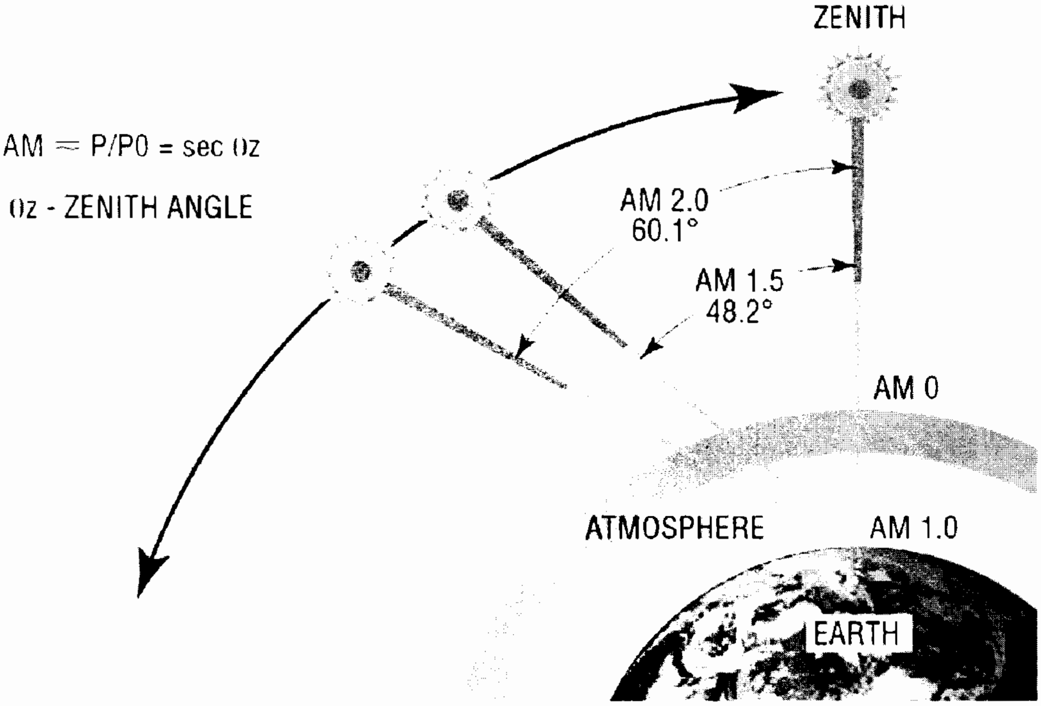

Figure 2.2 Variation of Air Mass with zenith angle [28]

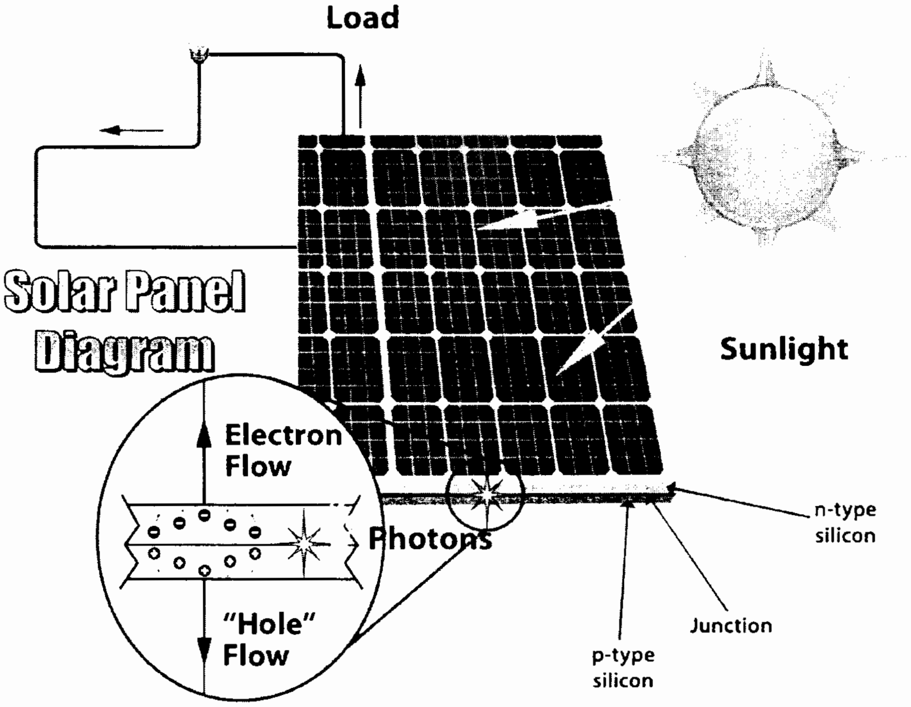

Figure 2.3 Simple diagram of a solar panel [29]

Table 2.1 Types of solar cells and their maximum reported efficiency (%) [28]

Solar cell	**Generation**	**Maximum reported efficiency (%)**
Silicon	1st generation (single crystal, single cell)	27.6 ± 1.0
CIGS	2nd generation (thin film, single cell)	20.3 ± 0.6
CdTe	2nd generation (thin film, single cell)	16.7 ± 0.5
DSSC	3rd generation (single cell)	11.2 ± 0.3
Organic polymer	3rd generation (single cell)	08.3 ± 0.3
GaAs/InGaAs/InGaP	Multi-junction cells (tandem cell)	42.3 ± 2.5

Dye-Sensitized Solar Cells

Basic Components of a DSSC

The dye-sensitized solar cell (DSSC) or the Gratzel cell has attracted a lot of interest for photovoltaic applications due to its relative low cost, easy and simple assembly.

Due to its nontoxicity, low cost and chemical stability under light irradiation, titanium dioxide (TiO_2) is often used as a photoanode in DSSC. The photosensitizer or dye molecules are absorbed unto the surface of the TiO_2 photoanode. Ruthenium (Ru) complex dyes developed by the Gratzel group are suitably used in DSSCs due to their wide range of absorption into the visible region (400 to 900 nm). A typical example of a Ru complex dye – the N3 dye (or red dye) is shown in Figure 2.4. The TCOG serves as substrate for the TiO_2 photoanode and for the counter electrode. For optimal performance the TCOG should have very low sheet resistance and high transparency. Fluorine-doped tin oxide (FTO) glass is usually used as the TCOG for DSSCs.

The redox electrolyte relays electrons between the TiO_2 photoanode and the counter electrode. For DSSCs electrolytes containing the tri- iodide/ iodide (I_3^-/I^-) redox couple are used. Platinum or carbon is usually used as the counter electrode in

DSSCs. The role of the counter electrode is to re-reduce tri- iodide ions into iodide ions.

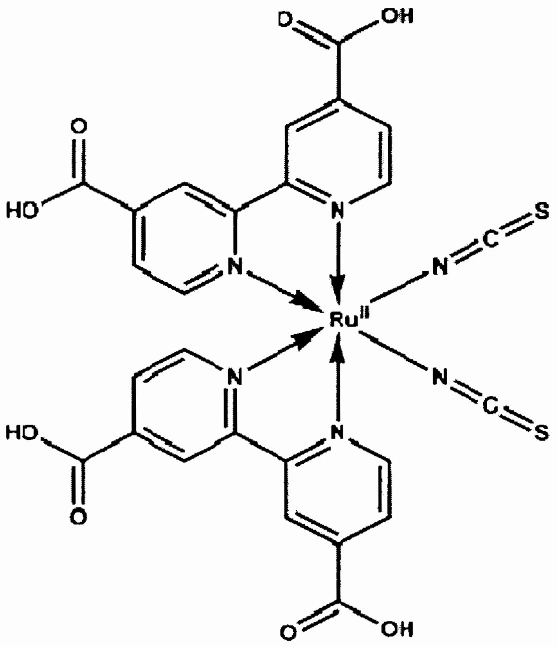

Figure 2.4 Chemical structure of N3 dye [26]

The basic components of a DSSC as shown in Figure 2.5, include a photoanode, photosensitizer or dye, transparent conducting oxide glass (TCOG), a redox electrolyte, and a counter electrode.

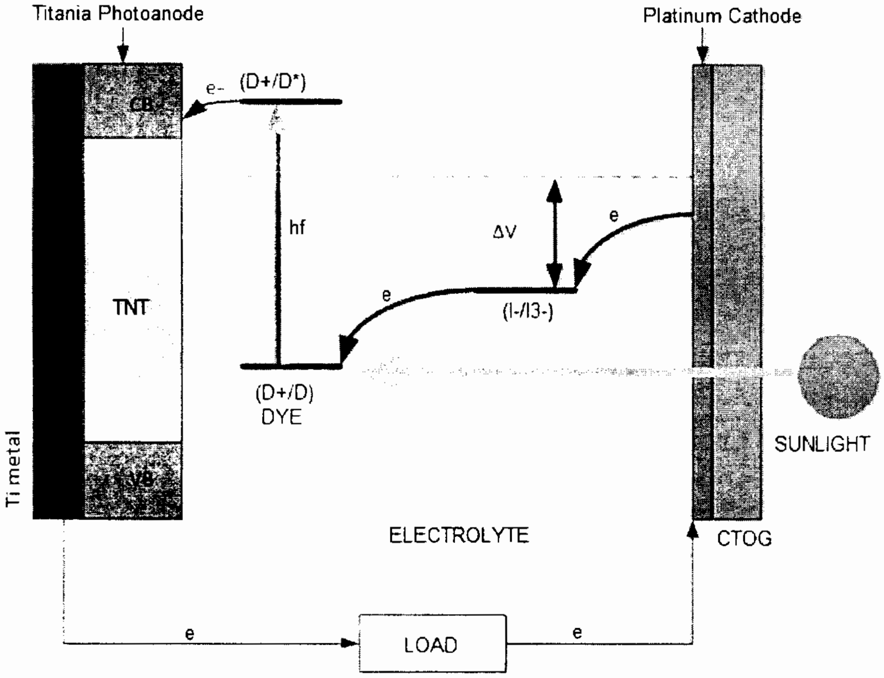

Figure 2.5 Components and working principle of a DSSC

Working principle of a DSSC

The dye molecules on the surface of the TiO_2 absorb photons of incident light and are excited from the ground state (D) to the excited state (D^*). The ground state corresponds to the HOMO of the dye while the excited state corresponds to the LUMO. The dye becomes oxidized when excited electrons jump into the conduction band (CB) of the TiO_2 photoanode. The electrons then diffuse through the TCOG to the load, and eventually tothecounter electrode. The oxidized dye (D^+) accepts electrons from iodide ions in the electrolyte and returns to the ground state (D). Meanwhile, the iodide is oxidized into tri-iodide ions. The tri-iodide ions diffuse to the counter electrode and are reduced back into iodide ions. The overall chemical reactions can be summarized as shown in equations 2.3 a, b, c and d (as adapted from [26]).

The four energy levels determining the performance of the DSSC are LUMO and HOMO of the dye, the Fermi level located near CB of the TiO_2 photoanode, and the redox potential of the electrolyte. The band gap energy for the cell $E_G = E_{HOMO} - E_{LUMO}$, determines the photocurrent generated by the cell. A large photocurrent is produced when E_G is small. We denote by ΔE_1, to be the energy gap between the LUMO and CB levels, while ΔE_2 is the energy gap between the HOMO level and the redox potential of the complex. For each of the electron transfer processes to be effective, the energy gaps $\Delta E_1 = E_{LUMO} - E_{CB}$ and $\Delta E_2 = E_{HOMO} - E_{RP}$ should exceed about 200 mV [26].

$$D + hf \rightarrow D^* \tag{2.3a}$$

$$D^* \rightarrow D^+ + e^- \tag{2.3b}$$

$$D^+ + e^- \rightarrow D \tag{2.3c}$$

$$I_3^- + 2e^- \rightarrow 3I^- \tag{2.3d}$$

Cell efficiency

The performance of a DSSC can be evaluated using the incident photon-to-current conversion efficiency (IPCE), the light harvesting efficiency (LHE), and the solar energy-to-electricity conversion efficiency (η). For a monochromatic radiation of wavelength λ, intensity I_o and generating a short-circuit photocurrent density J_{SC}, the IPCE can be obtained using the following equation:

$$IPCE = \frac{1240\, J_{SC}}{\lambda\, I_o} \times 100\ \% \tag{2.4}$$

A DSSC using an N3 dye could reach an IPCE of 80 % at 550 nm [26].

The solar power conversion efficiency (η) is the most widely used performance test for a solar cell. It is the ratio of the maximum output power P_m, to the power of the incident light P_{in}. It is usually obtained from the current-to-voltage characteristic (or IV Curve), as shown in Figure 2.6.

$$\eta = \frac{P_m}{P_{in}} \times 100\ \% = \frac{V_{OC} I_{SC} FF}{P_{in}} \times 100\ \% \tag{2.5}$$

Where, I_{sc} = short-circuit current density; V_{oc} = open-circuit voltage; and FF = fill factor.

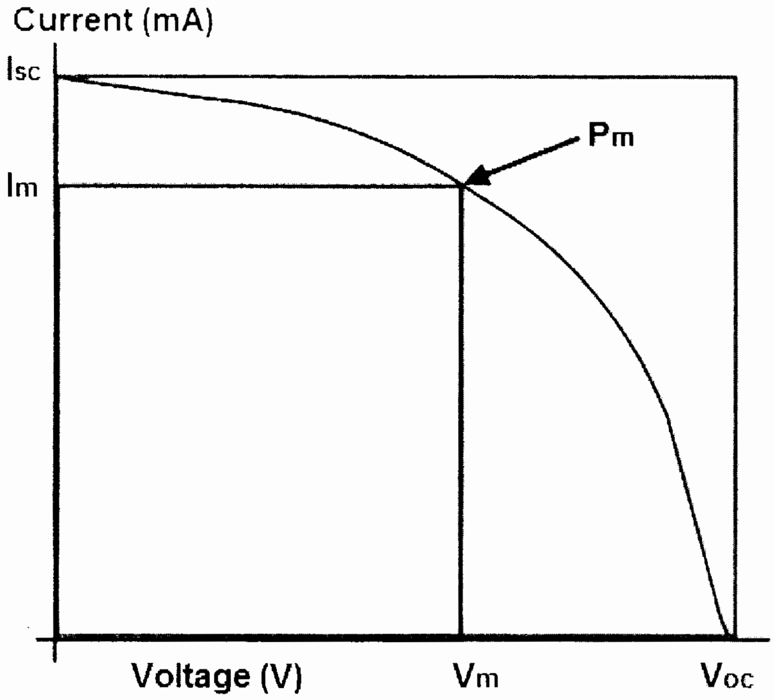

Figure 2.6 Typical current - voltage (I-V) characteristic for a solar cell

The fill factor gives a measure of the square-ness of the photocurrent versus voltage characteristic. If V_M and I_M are the operating voltage and current at maximum output power respectively, then the fill factor is given by

$$FF = \frac{V_M I_M}{V_{OC} I_{SC}} \tag{2.6}$$

Empirically, the fill factor can be expressed as [30]

$$FF = \frac{V_{OC} - \frac{kT}{q}\ln\left(\frac{qV_{OC}}{kT} + 0.72\right)}{V_{OC} + \frac{kT}{q}} \tag{2.7}$$

2.3 SEMICONDUCTOR BAND GAP AND SIZE DEPENDENT OPTICAL PHENOMENA

Semiconductor band gap

Based on their electrical properties, materials can be classified as insulators, conductors or semiconductors as shown in Figure 2.7. In a molecule, the highest occupied molecular orbital (HOMO) is referred to as the valence band, while the lowest unoccupied molecular orbital (LUMO) is referred to as the conduction band. The energy gap between the conduction band and the valence band is called the band gap energy E_G, given by $E_G = E_C - E_V$ [31]. This is illustrated in Figure 2.8a. A comparison of the band gap of different types of semiconductors is displayed in Figure 2.8b. In conductors the valence band (VB) and the conduction band (CB) overlap, resulting in high electrical conductivity. The band gap in insulators is very large, leading to high electrical resistivity. Semiconductors have a band gap lower than insulators, and therefore, have properties midway between conductors and insulators.

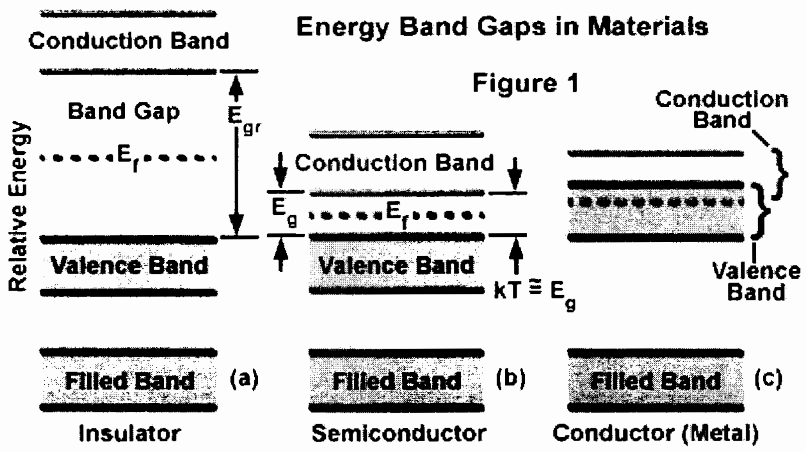

Figure 2.7 Comparison of band structure of insulators, conductors and semiconductors [32]

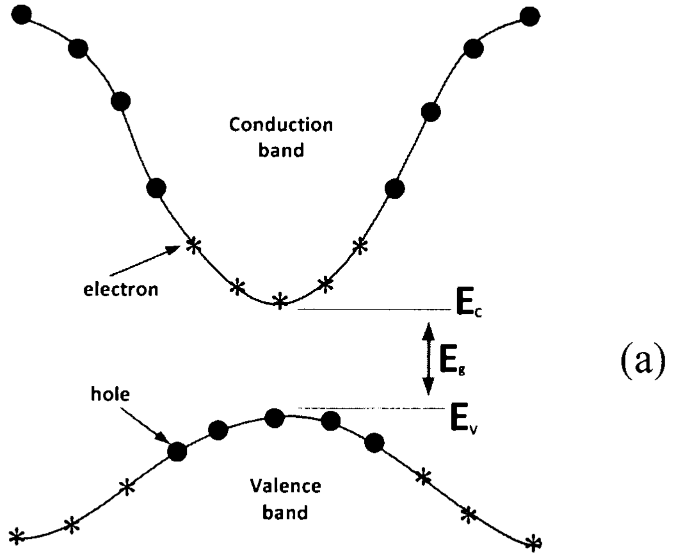

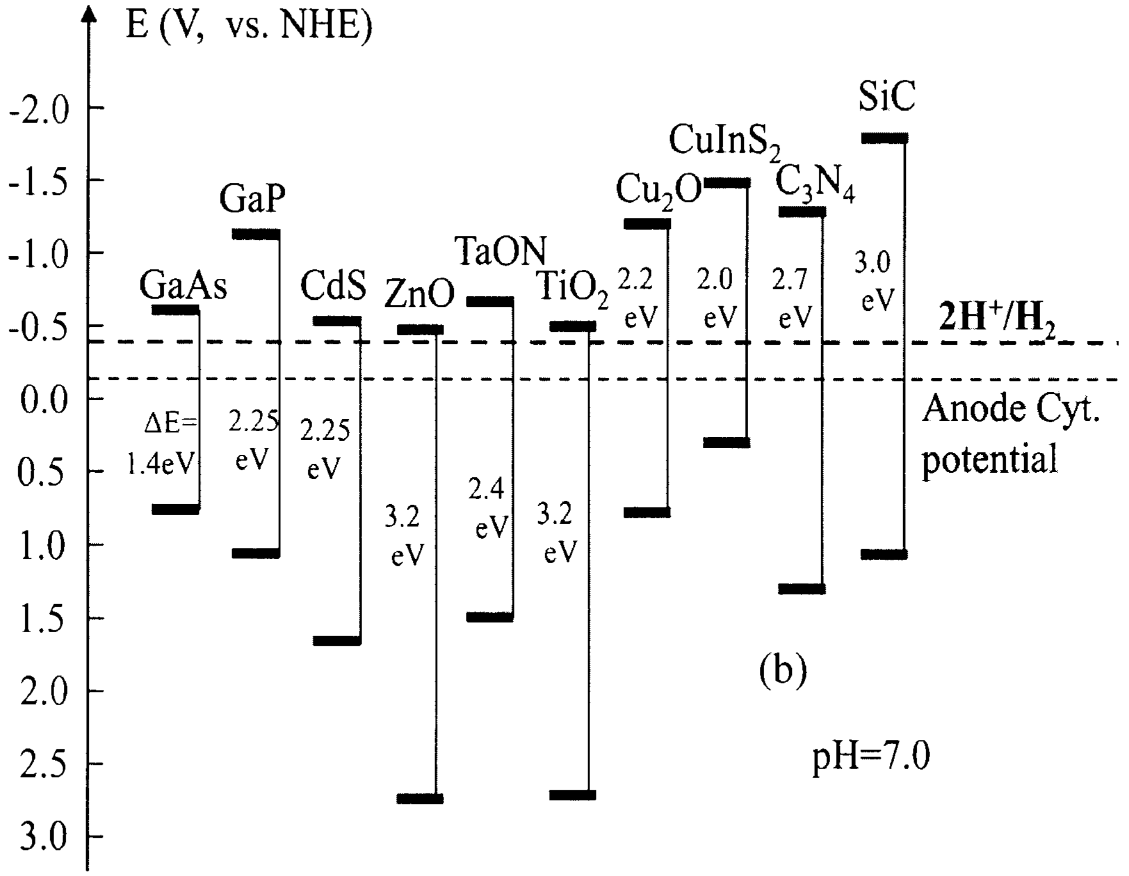

Figure 2.8 (a) Energy band gap of a semiconductor

(b) Energy band gap of some semiconductors [33]

The conductivity of semiconductors can be controlled be introducing impurity atoms or dopants, called donors (D) and acceptors (A). Depending on the type of donor or acceptor atoms, the semiconductor can be categorized as n-type or p-type. In n-type semiconductors, the electrons are the primary source of conduction, while in p-type semiconductors, the holes are the primary source of conduction.

When an n-type and a p-type semiconductor are brought into contact, a pn junction is formed. The diffusion of charge carriers (electrons and holes) across the junction causes unshielding of the fixed impurity charges – ionized donors in the n-type and ionized acceptors in the p-type. This in turn produces and electric field E and electric potential ϕ, which prevents further diffusion of charge carriers. Eventually, a space-charge region or depletion layer is formed which is devoid of free charges. See Figure 2.9.

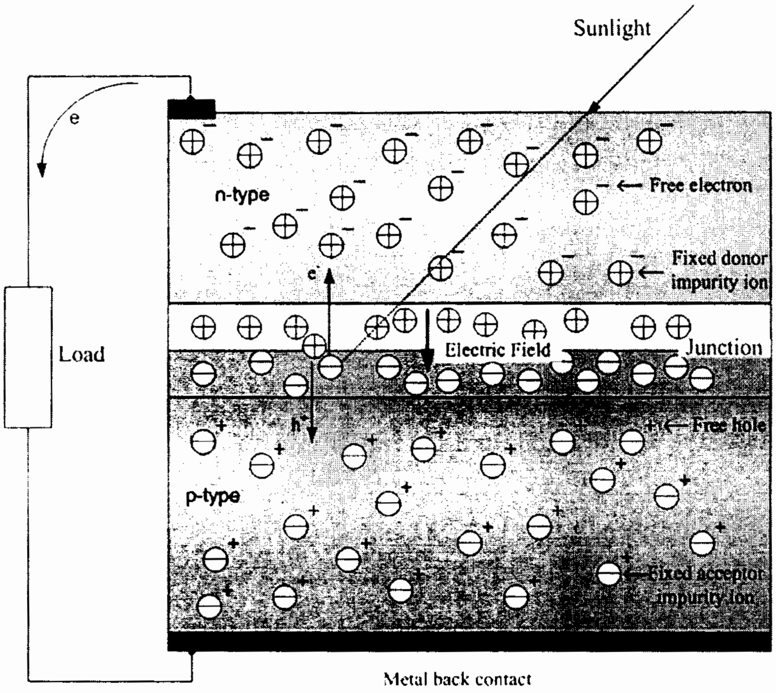

Figure 2.9 Depletion layer of a semiconductor formed around the pn junction

For single donor and acceptor levels at thermal equilibrium, solar cells and most semiconductor devices are governed by the Poisson's equation

$$\nabla.\vec{E} = \nabla^2\phi = \frac{q}{\varepsilon}(n_o - p_o + N_A^- - N_D^+) \tag{2.8}$$

Where ε = semiconductor electric permittivity, q = electronic charge, n_o and p_o are equilibrium electron and hole concentrations respectively, N_D^+ andN_A^- are the ionized donor and acceptor concentrations respectively. N_D^+ andN_A^- are given by [34]

$$N_D^+ = \frac{N_D}{1 + g_D e^{(E_F - E_D)/kT}} \tag{2.9}$$

$$N_A^+ = \frac{N_A}{1 + g_A e^{(E_A - E_F)/kT}} \tag{2.10}$$

Where E_F = Fermi energy, T = Kelvin temperature, k = Boltzmann's constant, E_D = donor energy of state, E_A = acceptor energy of state, N_D and N_A are the donor and acceptor concentrations respectively. The donor and acceptor degeneracy factors typically have the values $g_D = 2$ and $g_A = 4$. Figure 2.10 shows the donor and acceptor energy levels E_A and E_A in a semiconductor.

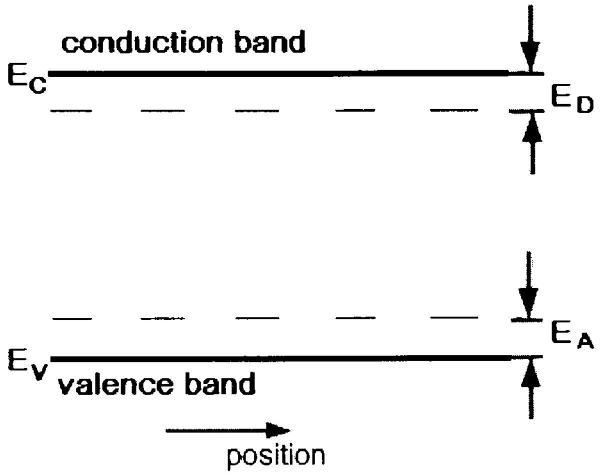

Figure 2.10 Diagram showing the donor and acceptor energy levels in a semiconductor

Semiconductors could be classified as direct band gap semiconductors (DBGS) or indirect band gap semiconductors (IBGS). In DBGS such as CdTe, GaAs and GaInP, the CB minimum and the VB maximum occur at the same crystal momentum value. Light absorption is mainly through photon absorption. See Figure 2.11. The absorption coefficient for direct transitions is given by [35]

$$\alpha \approx A\sqrt{hf - E_G} \tag{2.11}$$

Si and Ge are examples of IBGS, where the CB minimum and the VB maximum occur at different crystal momentum values. As shown in Figure 2.12, phonon absorption and phonon emission play a key role in light absorption, and the absorption coefficient $\alpha_a$and emission coefficient α_e are given by [35]

$$\alpha_a = \frac{B\left(hf - E_G + E_p\right)^2}{e^{E_p/kT} - 1} \tag{2.12}$$

$$\alpha_e = \frac{B\left(hf - E_G - E_p\right)^2}{1 - e^{-E_p/kT}} \tag{2.13}$$

The absorption coefficients are smaller for indirect transitions than for direct transitions. Hence, light penetration in IBGS is deeper than for DBGS.

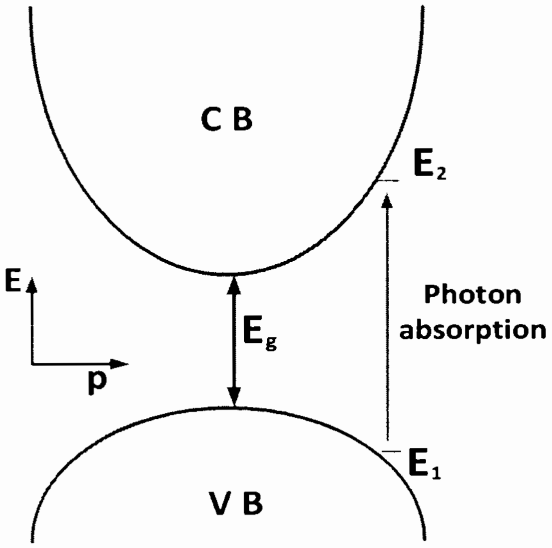

Figure 2.11 Photon absorption in a direct band gap semiconductor

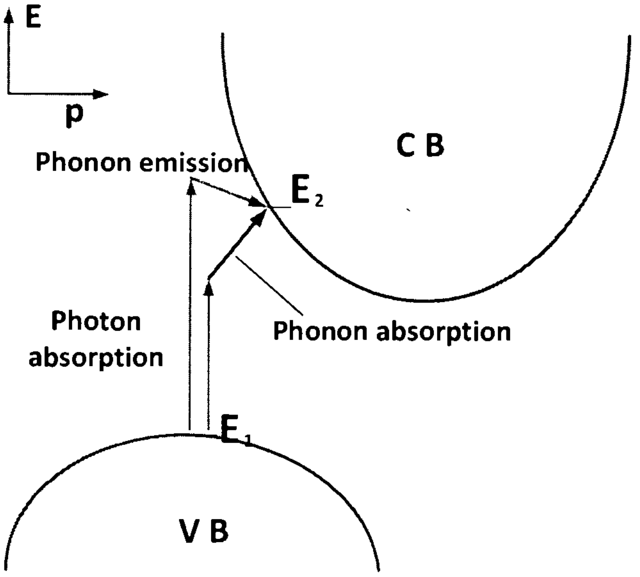

Figure 2.12 Absorption and emission in an indirect band gap semiconductor

Charge Recombination Processes

Recombination is the process by which electrons in the CB fall back to the VB and eliminate holes in the VB. Irradiation or current passing through a solar cell may disrupt the thermal equilibrium, and cause recombination. Figure 2.13 illustrates three common recombination mechanisms in solar cells - defects, band-to-band and Auger recombination processes.

Defects recombination or the Shockley-Read-Hall recombination occurs through traps in the forbidden gap. A single level trap (SLT) at energy E_T, with respective electron and hole concentration n and p, will have a net recombination rate per unit volume per second, given by [26]

$$R_{SLT} = \frac{pn - n_i^2}{\tau_{SLTp}[n + n_i e^{(E_T - E_i)/kT}] + \tau_{SLTn}[p + n_i e^{(E_i - E_T)/kT}]} \quad (2.14)$$

The carrier lifetime τ_{SLT} is inversely proportional to the recombination rate, and can be expressed in terms of the concentration of traps N_T, the thermal velocity v_{th} and the capture cross section σ, as

$$\tau_{SLT} = \frac{1}{\sigma v_{th} N_T} \tag{2.15}$$

In band-to-band or radiative recombination is more effective in DBGS. In the process, the electron energy is transferred to an emitted photon. Light emitting diodes and semiconductor lasers work on this principle. However, in IBGS, the electron energy is also given to a phonon. Given the lifetime τ_λ, the net radiative recombination rate can be expressed as

$$R_\lambda = \frac{pn - n_i^2}{n_o \tau_\lambda} \tag{2.16}$$

In Auger recombination, the transition energy is given to another carrier electron or hole in the CB or VB. This carrier then liberates its excess momentum and energy to a phonon. The net Auger recombination rate can be expressed in terms of minority lifetimesτ_A as

$$R_A = \left[\frac{n}{\tau_{A,p}} + \frac{p}{\tau_{A,n}}\right]\left[\frac{pn - n_i^2}{n_o^2}\right] \tag{2.17}$$

These recombination processes may occur simultaneously, and the total rate of recombination R in the forbidden gap with multiple traps is given by

$$R = \left(\sum R_{SLT}\right) + R_\lambda + R_A \tag{2.18}$$

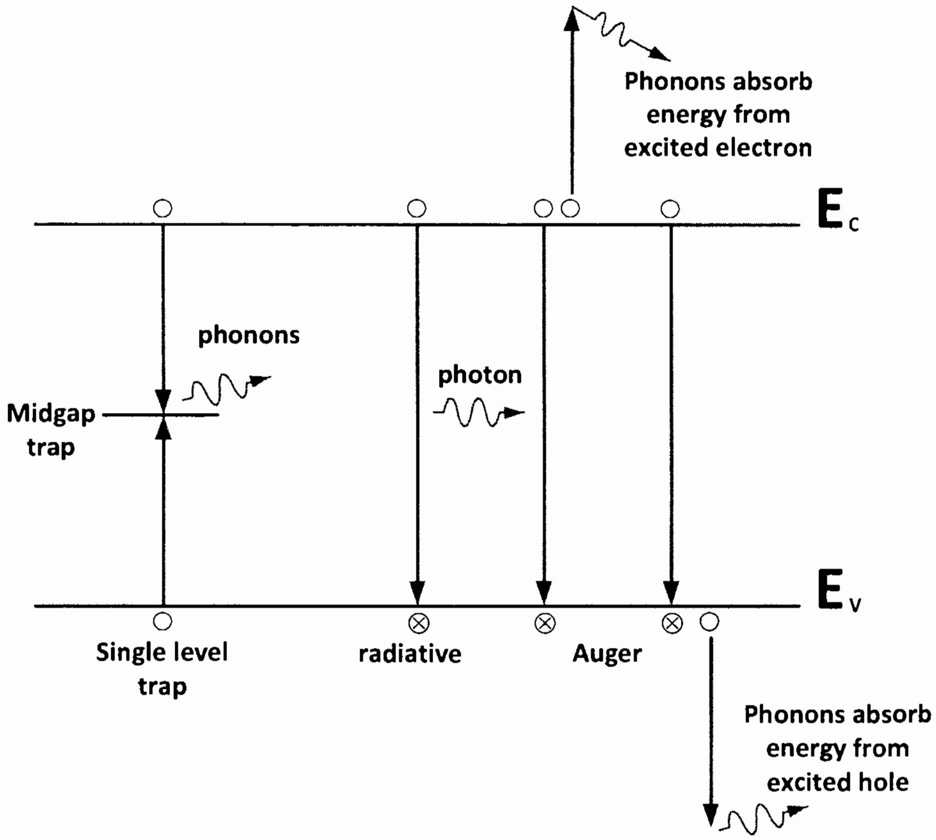

Figure 2.13 Three common recombination mechanisms in solar cells

Surface Plasmon Resonance

Surface plasmon resonance (SPR) is generated when the size of a nanomaterial is smaller than the wavelength of the incident radiation. The electric field of the incident light polarizes the free conduction electrons relative to the lattice cation. This is illustrated in Figure 2.14. The restoring force is provided by the net charge difference at the surface of the nanomaterial. A dipolar oscillation or excitation is thus created with a given frequency. This frequency depends on particle size, as seen in Figure 2.15. The energy of the SPR is a function of the electron density and the dielectric ε_o of the surrounding medium. The resonance width depends on the time before electron scattering occurs. For a spherical nanoparticle with radius r, dielectric ε_i, the scattering and extinction coefficients of incident light with wavelength λ are given by [36]:

$$Q_{sca} = \frac{8\varepsilon_o^2}{3}\left(\frac{2\pi r}{\lambda}\right)^4 \left|\frac{\varepsilon_i - \varepsilon_o}{\varepsilon_i + 2\varepsilon_o}\right|^2 \tag{2.19}$$

$$Q_{ext} = \frac{8\pi r\sqrt{\varepsilon_o}}{\lambda} Im\left(\frac{\varepsilon_i - \varepsilon_o}{\varepsilon_i + 2\varepsilon_o}\right) \tag{2.20}$$

The absorption coefficient is the difference between the extinction and scattering coefficients

$$Q_{abs} = Q_{ext} - Q_{sca} \tag{2.21}$$

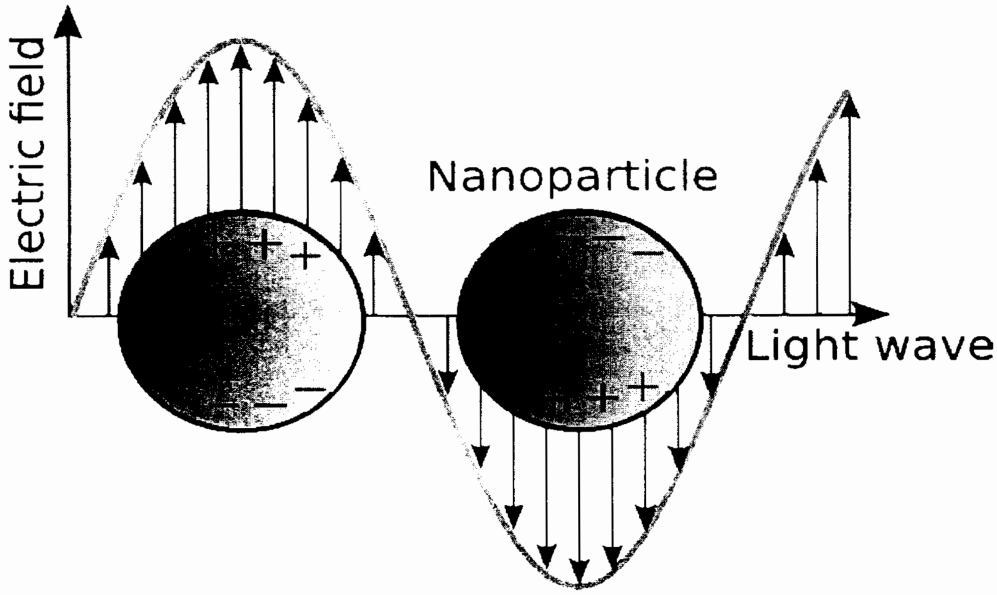

Figure 2.14 Induced polarizations of free electrons in a nanomaterial leading to SPR [37]

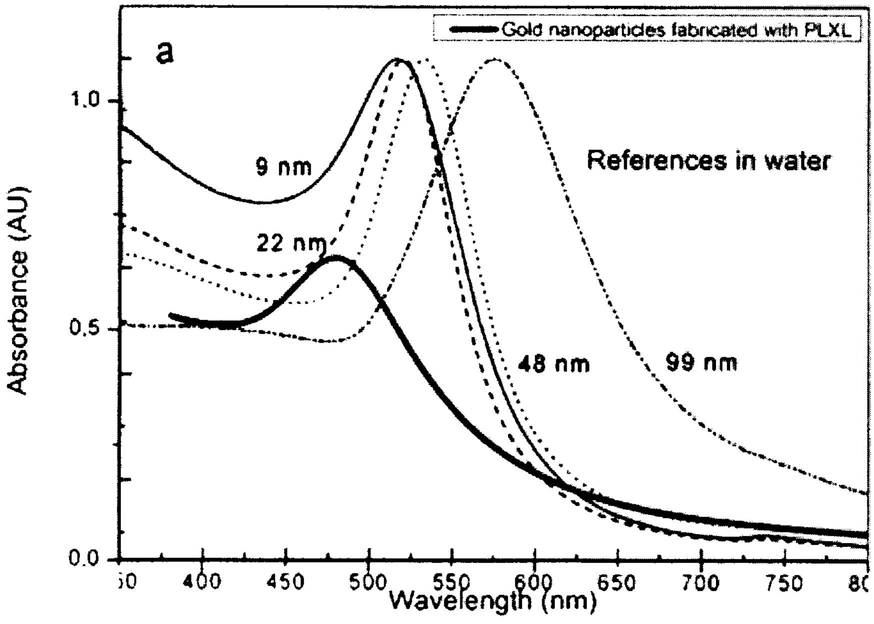

Figure 2.15 Size dependence of plasmon excitation frequency of gold nanoparticles [38]

Quantum Size Effect

When the size of a nanomaterial is smaller than the de Broglie wavelength, confinement of electrons and holes leads to the formation of electric dipoles and discrete electronic states. As illustrated in Figure 2.16, discretization of the energy states increases as size of the material decreases. For semiconductor nanomaterials, the band gap also increases as size of the material decreases. The result is a shift in interband transition towards higher frequencies. Figure 2.17 also shows decrease of energy band gap when the size of ZnSe QD deceases.

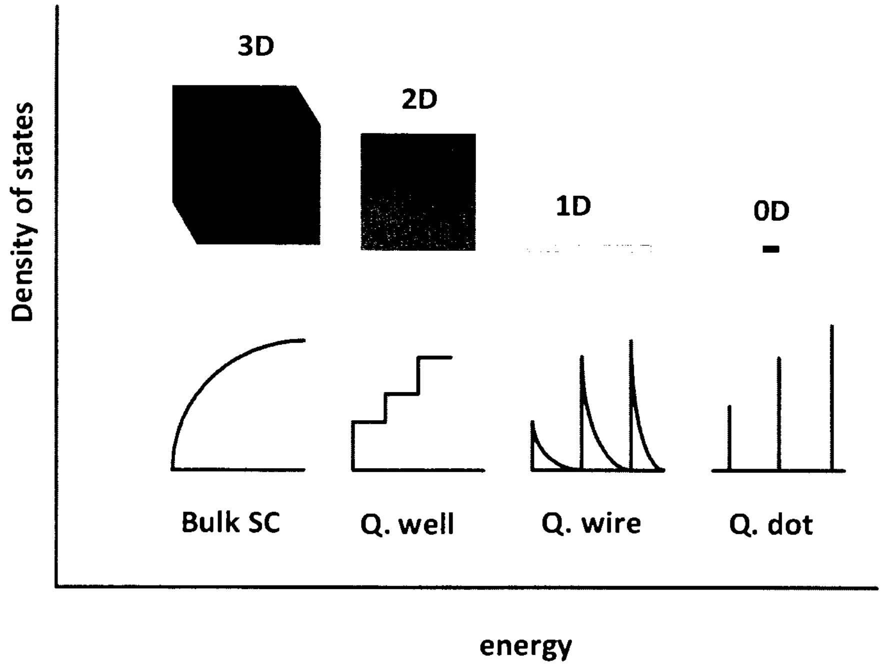

Figure 2.16 Diagram showing discretization of electronic states as function of size [37-38]

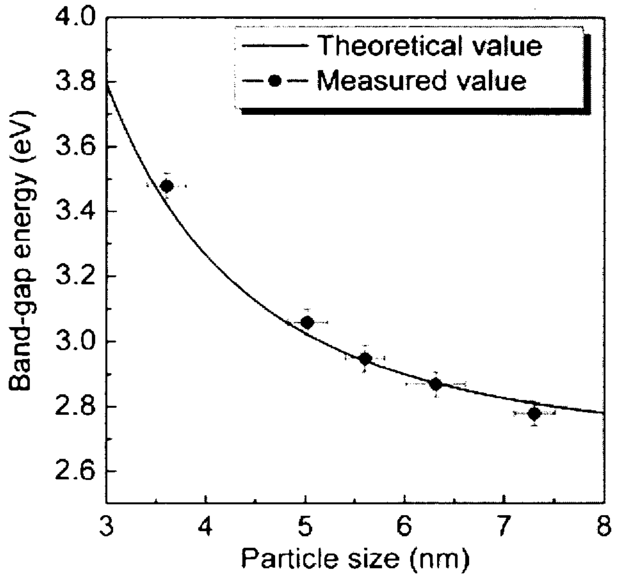

Figure 2.17 Energy band gap of ZnSe QD as a function of size [38]

2.4 PROPERTIES OF TITANIUM DIOXIDE

Crystal Structure

Titanium dioxide (TiO_2) or Titania occur naturally in three major crystalline phases or polymorphs – rutile, anatase and brookite. These phases are shown in Figure 2.18. The basic unit of each polymorph consists of a titanium atom surrounded by six oxygen atoms in a rather distorted TiO_6 octahedral configuration. The assembly patterns of the octahedral chain and the degree of distortion of each octahedral account for the differences in crystal structure.

In rutile, neighboring TiO_6 units share corners, and are stacked with their long axis alternating by 90°. Anatase framework consists of strongly distorted edge sharing TiO_6 octahedral. Corner sharing and edge sharing octahedral units give rise to the three-dimensional network of brookite. Differences in mass density and electronic band structure are explained in terms of the different lattice structure. Figure 2.19 shows a comparison of optical band gap of TiO_2 phases.

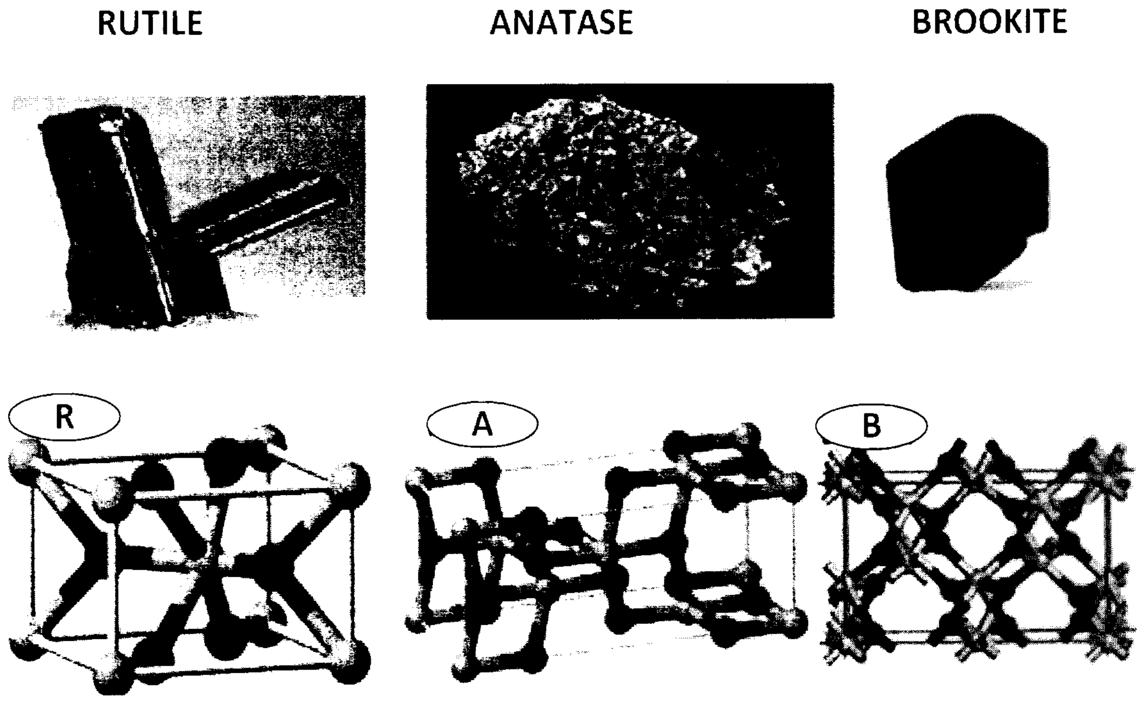

Figure 2.18 Crystalline phases of TiO_2 (R = rutile, A = anatase, B = brookite)
[39]

Table 2.2 gives a summary of other properties of Titania crystal phases. The anatase and brookite phases are thermodynamically less stable than the rutile phase and undergo phase transformation at high temperatures. Due to its crystal and electronic structure, anatase is the most photoactive form of Titania. The high light scattering property of rutile makes it suitable for applications such as paint pigments. The low photcatalytic activity, low stability and complex preparation method for brookite, makes it the least used form of titania.

Table 2.2 Properties of titania crystal phases - rutile, anatase and brookite [40-43]

Properties	**Rutile**	**Anatase**	**Brookite**
Crystal structure	Tetragonal	Tetragonal	Orthorhombic
Molar mass (g/mol)	79.87	79.87	79.87
Density (kg/m^3)	4240	3830	4170
Band gap (eV)	3.0	3.2	3.4
Permittivity	114	48	78
Refractive index	2.95	2.57	2.81
Mohs' hardness	7.0 – 7.5	5.5 – 6.0	5.5 – 6.0
Lattice constant (Å)	a = 4.59, c = 2.96	a = 3.78, c = 9.52	-
Light absorption (nm)	< 415	< 390	-

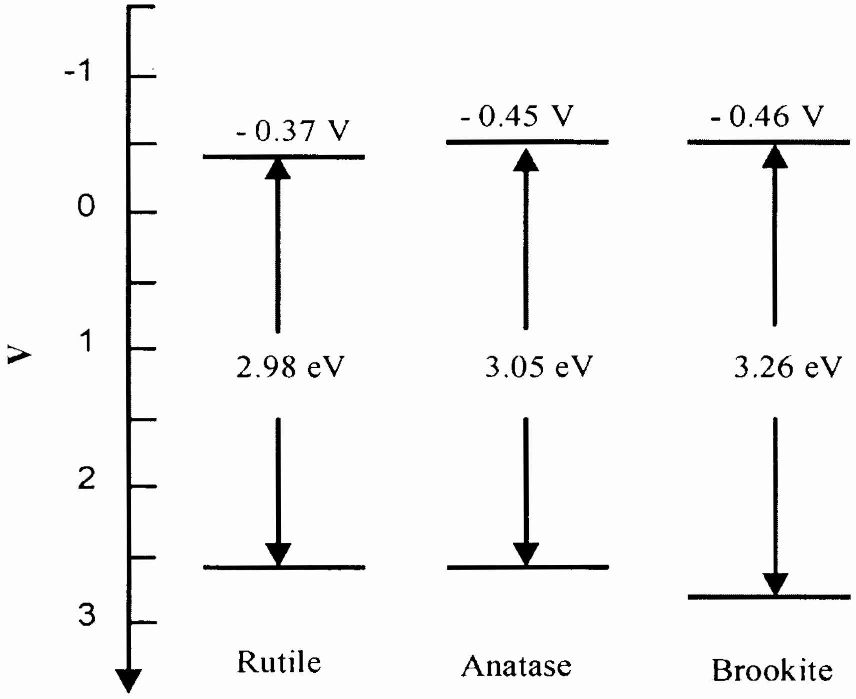

Figure 2.19 Comparison of optical band gap of TiO_2 phases [44]

Amorphous anatase can convert to crystalline anatase with heat treatment of at least 280 °C. A mixture of anatase and rutile will undergo conversion at temperatures higher than 430 °C. Figure 2.20 shows X-ray diffraction pattern, which indicates the formation of nanocrystalline TiO_2 nanotubes after annealing or calcination at temperatures ranging from 230 °C to 880 °C in dry oxygen ambient for three hours.

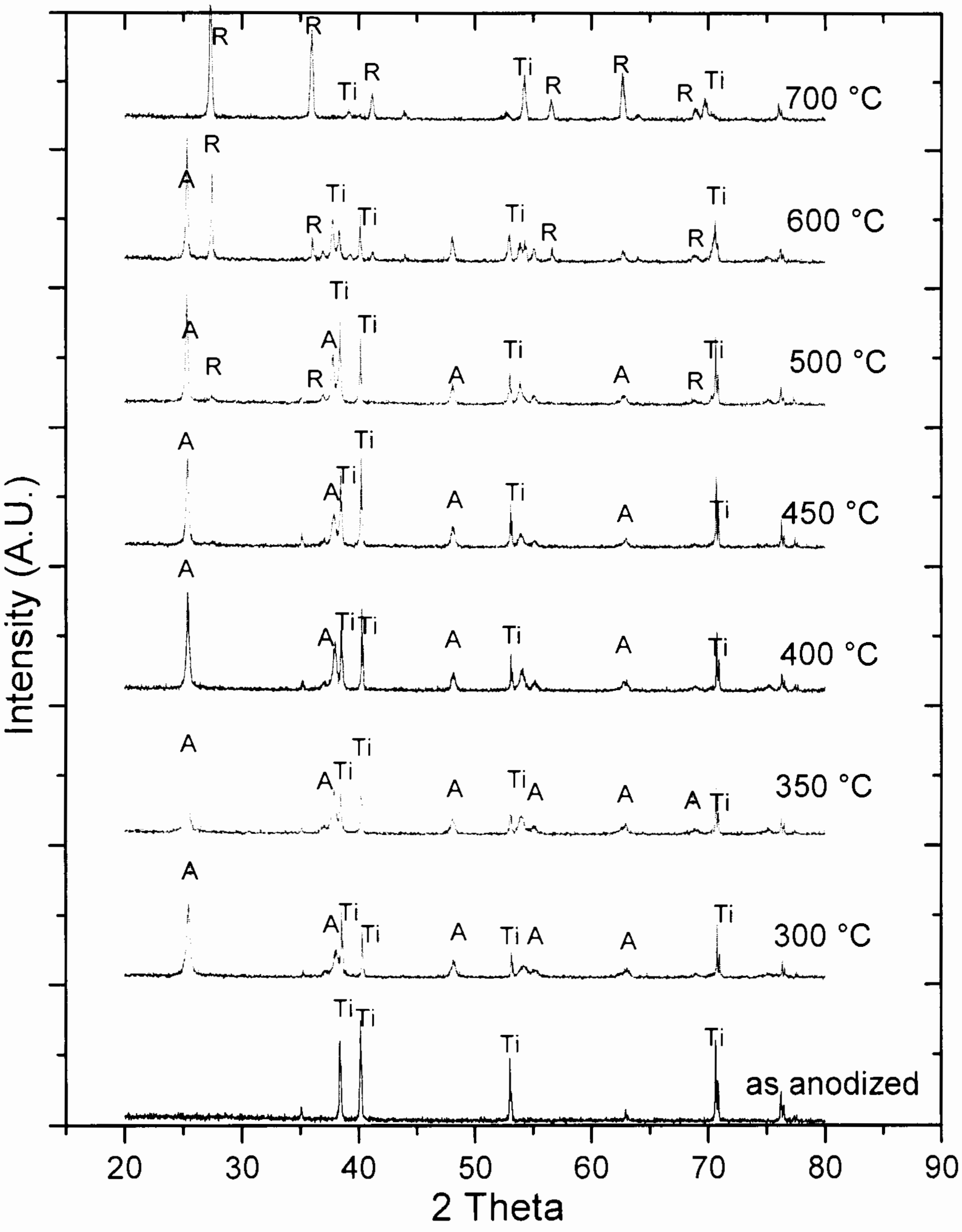

Figure 2.20 XRD patterns of crystalline phases of nanocrystalline TiO_2 after calcination at different temperatures in air for 2 h [18]

The bulk structure of titania networks is quite complex with various types of intrinsic defects including oxygen vacancies. Such oxygen deficiency implies the presence of some Ti (III) centers that behave like electron-donating species, providing an n-type character to the semiconductor.

Physical Properties of TiO_2

Table 2.3 Physical Properties of titania [40, 42, 43]

Properties	**Values**
Melting point	1843 °C
Boiling point	2972 °C
Thermal expansivity	9×10^{-6} (r.t - 1000 °C)
Thermal conductivity	11.7 Wm/k (25 °C)
Resistivity	10^{12} Ω cm (25 °C) ; 2.5×10^{4} Ω cm (700 °C)
Dielectric constant	85 (1MHz)
Modulus of Elasticity	230 GPa
Modulus of Rupture	140 MPa
Shear Modulus	90 GPa
Micro Hardness	880 (HV0.5)
Compressive strength	680 MPa
Fracture toughness	3.2 $MPa/m^{-1/2}$
Poisson's ratio	0.27
Porosity	0 %
Latent heat of fusion	930 kJ/kg
Specific heat	697 J/kg.k

Table 2.3 shows some physical properties of titania. It should be noted that these properties may vary depending grain size and on method of preparation.

2.5 STRUCTURAL MODIFICATION OF TIO_2

TiO_2 is a wide band gap semiconductor (3.2 eV for anatase) as seen in Figure 2.19 and Table 2.2. This limits absorption of solar energy to the UV region, resulting in low solar energy conversion efficiency. To shift absorption into the visible region requires narrowing of the band gap. The narrowing of the band gap also presents another problem – the recombination of electron-hole pairs. Two effective ways to solve these problems is by using nanotubes of TiO_2 and by doping TiO_2 with a foreign element.

Nanotubes

Nanotubes or quantum wires are 1D nanomaterials in which the motion of electrons and holes is allowed in one direction only. In all 1D nanostructures (nanotubes, nanorods, nanowires and nanofibers), quantum effects control transportation in the other two dimensions which are comparable to the Bohr exciton radius. Due to confinement, the transverse energies of the electrons are quantized. In simple terms, the wave function and quantized energy can be expressed as follows [37]

$$\Psi = \sqrt{\frac{4}{L_x L_y}} sin\left\{\left(\frac{n_x \pi x}{L_x}\right)\left(\frac{n_y \pi y}{L_y}\right)\right\} \tag{2.22}$$

$$E = \frac{\hbar^2 \pi^2}{2m}\left\{\left(\frac{n_x}{L_x}\right)^2 + \left(\frac{n_y}{L_y}\right)^2\right\} \tag{2.23}$$

For application in DSSCs, TiO_2 nanotubes have several advantages over TiO_2 nanoparticles in that, their 1D structure helps to limit transportation in one direction only and reduce recombination of the photo-injected electrons. In addition, their tubular structure offers a large surface area for absorbing dye molecules and capturing incident photons [9]. Figure 2.21 shows SEM image of TiO_2 nanotubes.

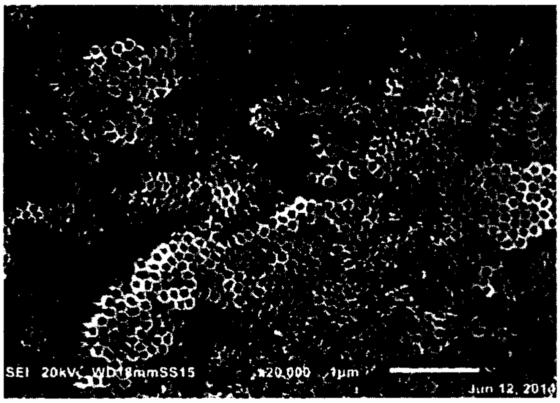

Figure 2.21 SEM image of TiO_2 nanotubes [83]

Doping TiO_2

One of the most promising ways to improve the optical responds of TiO_2 is by doping with foreign ions. Dopant ions can reduce the rate of recombination through the introduction of charge traps for either electrons, or holes, or both [4]. In addition, dopant ions can cause formation of mid-band gaps, and effective band gap reduction (BGR) at high concentrations. As shown in Figure 2.22 the photon absorption of undoped TiO_2 can be extended from over 3 eV to about 2 eV by doping with foreign ions.

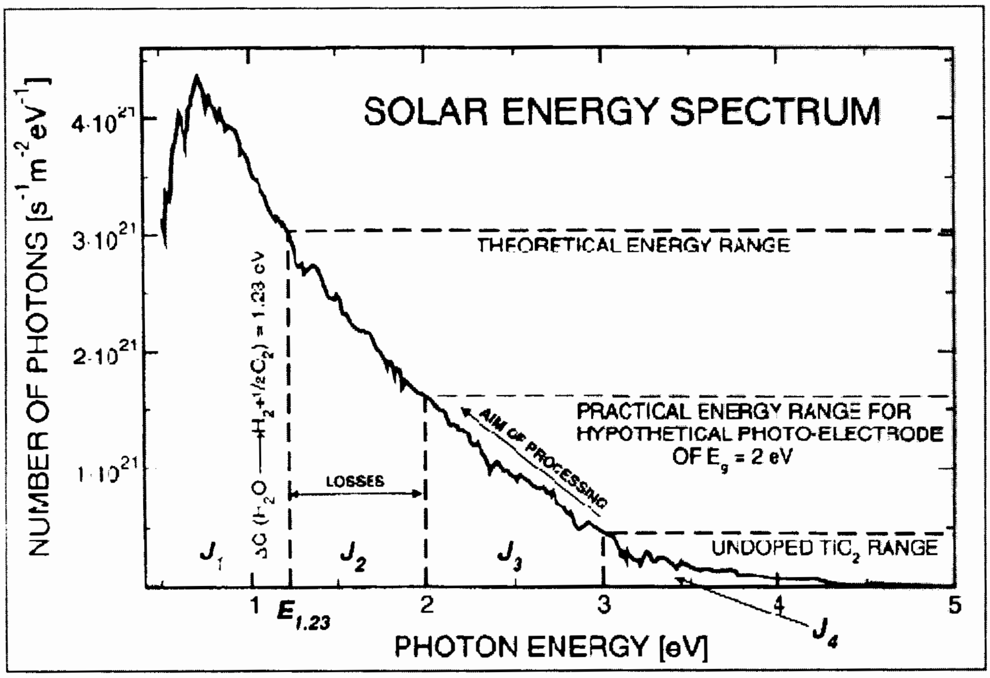

Figure 2.22 Solar energy spectrum and photon absorption for undoped TiO_2 and modified TiO_2 [45-46]

In 2011, Charles Dunnill and Ivan Parkin [47] were able to successfully reduce the band gap of TiO_2 anatase from 3.2 eV to 2.46 eV by doping with Nitrogen. Their result is illustrated in Figure 2.23.

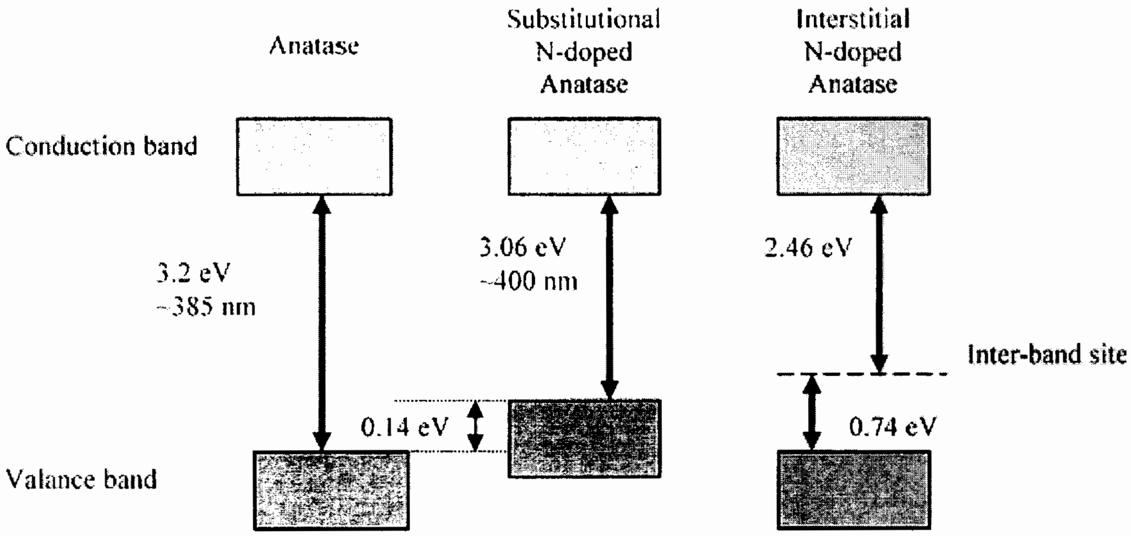

Figure 2.23 Band gap narrowing of Nitrogen-doped TiO_2 [47]

2.6 DC ANODIZATION MECHANISM AND FORMATION OF TIO_2 NANOTUBES

Self-organized TiO_2 nanotubes can be obtained by DC anodization in a Fluoride electrolyte solution. The nanotubes are formed at the anode, on a titanium sheet. Platinum is commonly used as the cathode. The diagram of simple DC anodization set-up is shown in Figure 2.24.

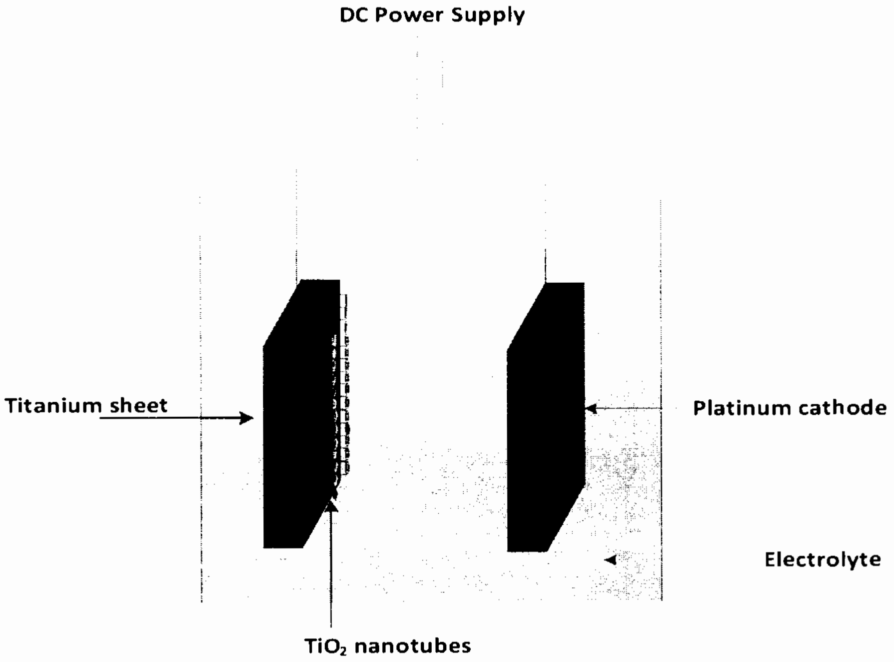

Figure 2.24 Diagram of DC Anodization apparatus

Step 1: Formation of an oxide layer

When a DC voltage is applied in through the electrolyte, a compact oxide layer begins to form on the surface of the Ti metal sheet due to interaction of the metal with O^{2-} or OH^- ions [48-51]. Pore nucleation begins to appear on the oxide layer. Figure 2.25 illustrates the oxide layer formation and the associated chemical reaction.

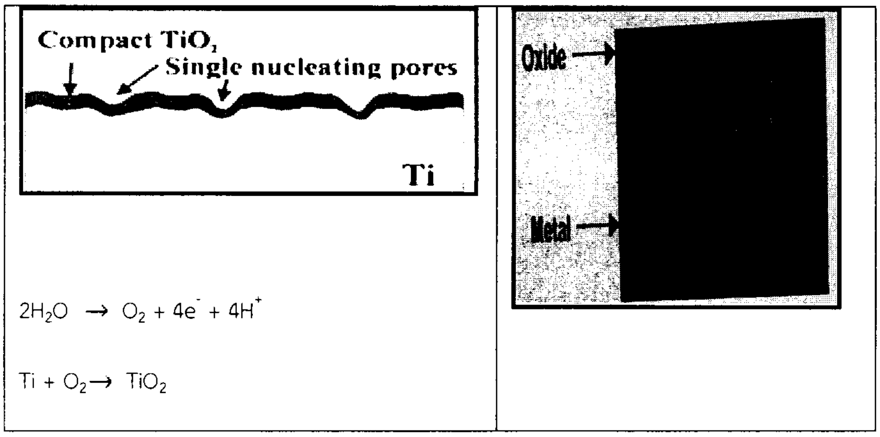

$2H_2O \rightarrow O_2 + 4e^- + 4H^+$

$Ti + O_2 \rightarrow TiO_2$

Figure 2.25 Illustration of oxide layer formation [50]

Step 2: Dissolution and pore growth

The compact oxide begins to dissolve and dissolution takes place only in selected areas due to differential stress. Dissolution of TiO_2 as soluble $[TiF_6]^{2-}$ occurs and makes the pores grow deeper [48-51]. Ti^{4+} ions migrate from the metal/oxide interface to the oxide/electrolyte interface assisted by the electric field or NH_4F solution, resulting in etching of the oxide layer. Figure 2.26 illustrates dissolution, pore growth and the associated chemical reaction.

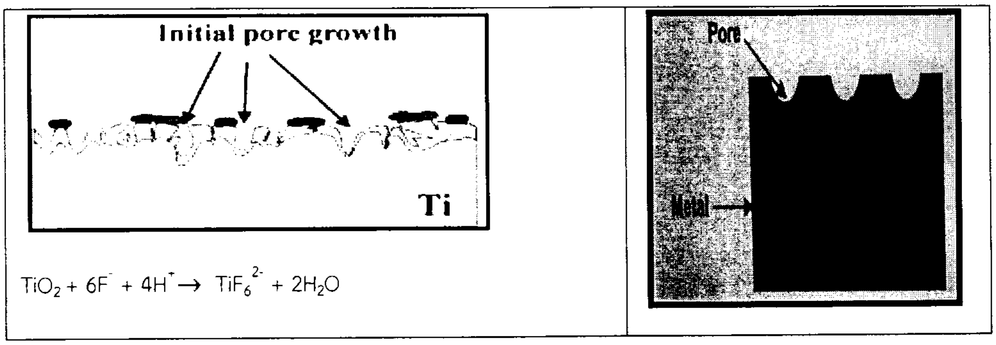

$TiO_2 + 6F^- + 4H^+ \rightarrow TiF_6^{2-} + 2H_2O$

Figure 2.26 Illustration of dissolution and pore growth [50]

Step 3: Field assisted dissolution

Selective etching and localized field assisted dissolution gives rise to pore growth and eventual formation of a pore layer. The Ti-O bond is polarized and weakened by the electric field to accelerate the dissolution of Ti^{4+} cationsinto the electrolyte. The free O^{2-} anions move to the metal/oxide interface to react with the metal. At the bottom of the pore, the oxide layer moves inward and cause further growth of the pore. This is shown in Figure 2.27a,c. The oxide growth rate and the oxide dissolution rate eventually balanced up. At this point, the barrier layer moves further in to form deeper pores without any change in its thickness [48, 49, 50]. Deeper pores give rise to increase in the electric field, and enhance field assisted oxide growth and oxide dissolution. As illustrated in Figure 2.27 b,d, voids begin to form around the pores.

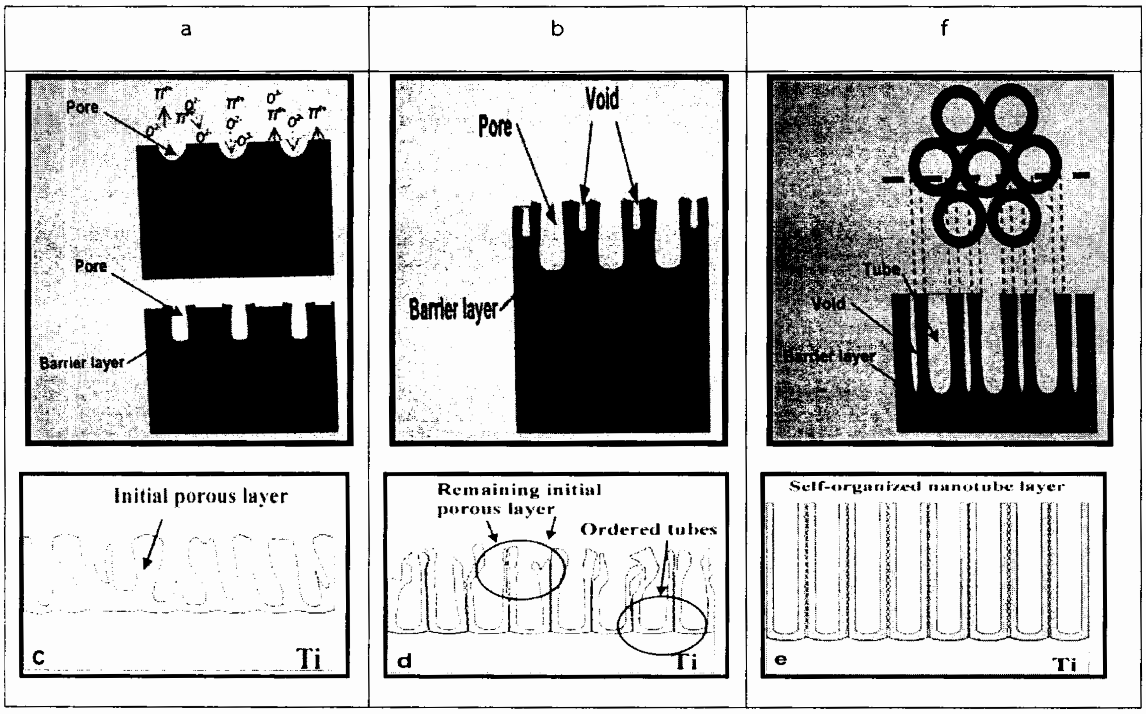

Figure 2.27 Field assisted dissolution and formation of self-organized nanotube arrays [50]

The NH_4F electrolyte favors development of the nanopores into nanotubes. As the nanotubes and voids grow in equilibrium, a tubular array is established. Oxidation and dissolution reduces the barrier layer thickness and keeps the etching process active. The ultimate result is formation of self-organized nanotube arrays as shown in Figure 2.28 f,e.

CHAPTER 3

EXPERIMENTAL PROCEDURES

This chapter covers the synthesis of N-doped TiO_2 nanotubes, characterization techniques used (XRD, SEM, UVS, EDX and XPS), and testing of each sample's performance in a dye - sensitized solar cell (DSSC). The experimental procedures are summarized in Figure 3.1.

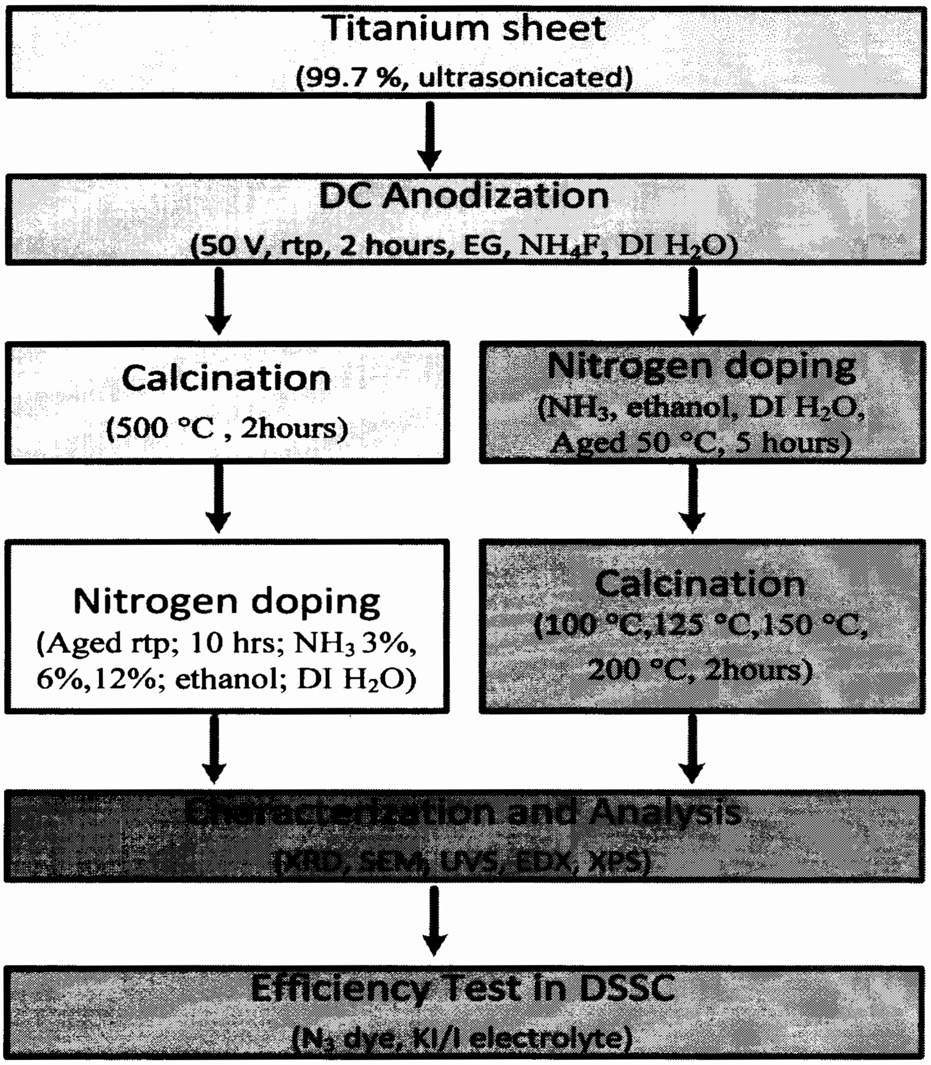

Figure 3.1 Chart summarizing the experimental procedures for this research

3.1 PREPARATION OF NITROGEN - DOPED TIO_2 NANOTUBES

Preparation of TiO_2 nanotubes

In this research the TiO_2 nanotubes were prepared by DC anodization at room temperature on titanium sheet of thickness 0.2 mm, of diameter 1 cm and 99.7 % purity, purchased from Sigma Aldrich. Before anodization, the sheet was first polished and ultrasonicated for 10 minutes in isopropanol, de-ionized water and ethanol. The electrolyte solution which consist of ethylene glycol (EG), ammonium fluoride (0.3 % wt NH_4F) and deionized water (2 % vol DI H_2O), was stirred magnetically for 2 hours and kept for 5 hours prior to anodization. The Ti sheet is mounted to serve as the anode in the electrolyte, while the cathode or counter electrode is made of platinum. A constant 50 V DC voltage is applied during anodization and each sample is anodized for 2 hours. The anodization set up is shown in Figure 3.2.

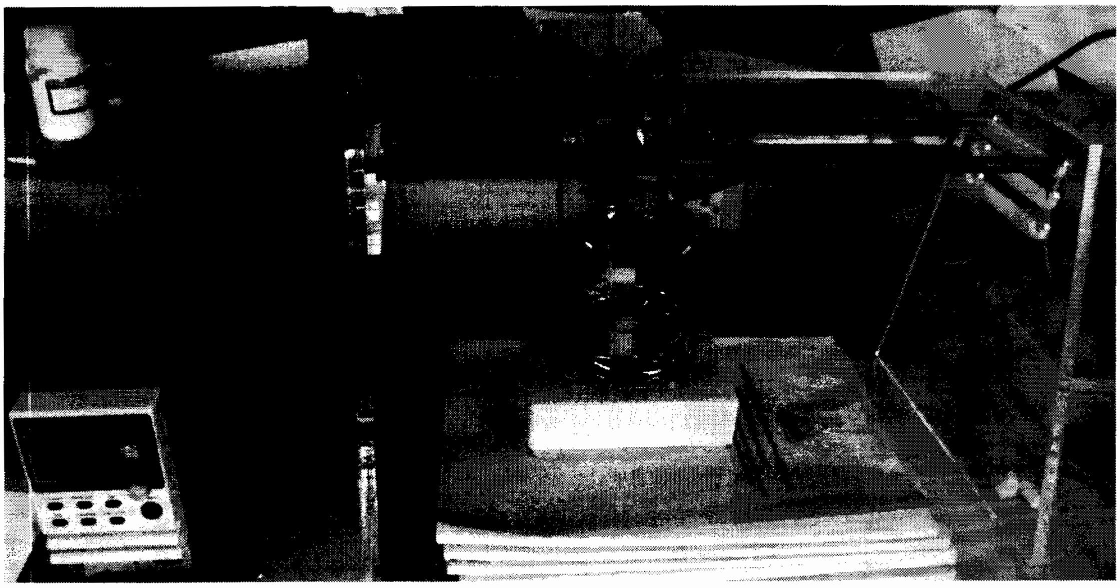

Figure 3.2 DC Anodization apparatus

Doping TiO_2 nanotubes with Nitrogen

Two sets of Nitrogen - doped TiO_2 nanotubes (N-TNT) were prepared. In set 1, the concentration of the dopant was varied, while in set 2 the calcination temperature was changed.

N-TNT Set 1

After preparation of the TiO_2 nanotubes, the samples were calcinated at 500 °C for 2 hours, and aged in a mixture containing ethanol, 30 % vol DI H_2O, and 1M ammonia solution (NH_3) as source of nitrogen. It is reported that above 450 °C, total phase transformation from amorphous into crystalline [15, 18], hence, the choice of calcination at 500 °C. The volume of NH_3 was varied (1 %, 3 %, 6 % and 12 %) and each sample was aged for 10 hours at room temperature. The samples were then ultrasonicated and dried in air.

N-TNT Set 2

The as-prepared TiO_2 nanotubes were aged in a mixture containing 65 % vol ethanol, 30 % vol DI H_2O, and 5 % vol 1M ammonia solution (NH_3) as source of nitrogen. The samples were aged for 5 hours at 50 °C, and then ultrasonicated for 10 minutes. It is expected that higher temperature aging will increase the kinematics of ion mobility and promote faster incorporation of dopant element into the TiO_2 lattice. Much higher temperatures may lead to greater surface deposition rather than penetration. This is the reason for the choice of a moderately high aging temperature of 50 °C. Finally the samples were calcinated for 2 hours at different temperatures (100 °C, 125 °C, 150 °C and 200 °C).

3.2 CHARACTERIZATION TECHNIQUES

The prepared samples were characterized using several techniques - X-ray Diffraction (XRD), Scanning Electron Microscopy (SEM), UV-Visible light Spectroscopy (UVS), Energy Dispersive X-ray Spectroscopy (EDX), and X-ray Photoelectron Spectroscopy (XPS).

X-ray Diffraction (XRD)

The XRD was be performed to determine the crystal phase and crystallite size of the samples using a Philips X'Pert-MDP X-ray diffractometer (shown in Figure 3.3) with Cu - K_α radiation ($\lambda = 1.5418$ Å) with Ni filter. The operational mode was 40 kV, 35 mA, with spectral scanning in the 2θ range from (20°-80°) at a rate of 0.02° per second. Figure 3.4 shows a schematic diagram of how the X-ray Diffractometer operates.

Crystallite Size D

Information about the crystal size D can be obtained from the XRD peaks. Given the X-ray wavelength (λ), the Bragg angle for the most prominent diffraction peak (θ), measurement of the full width half maximum (β), the crystallite size can be calculated using the Scherrer equation [37, 38]:

$$D = \frac{\gamma\lambda}{\beta cos\theta} \tag{3.1}$$

Usually, $\gamma = 0.9$, and is called the shape factor or Scherrer constant.

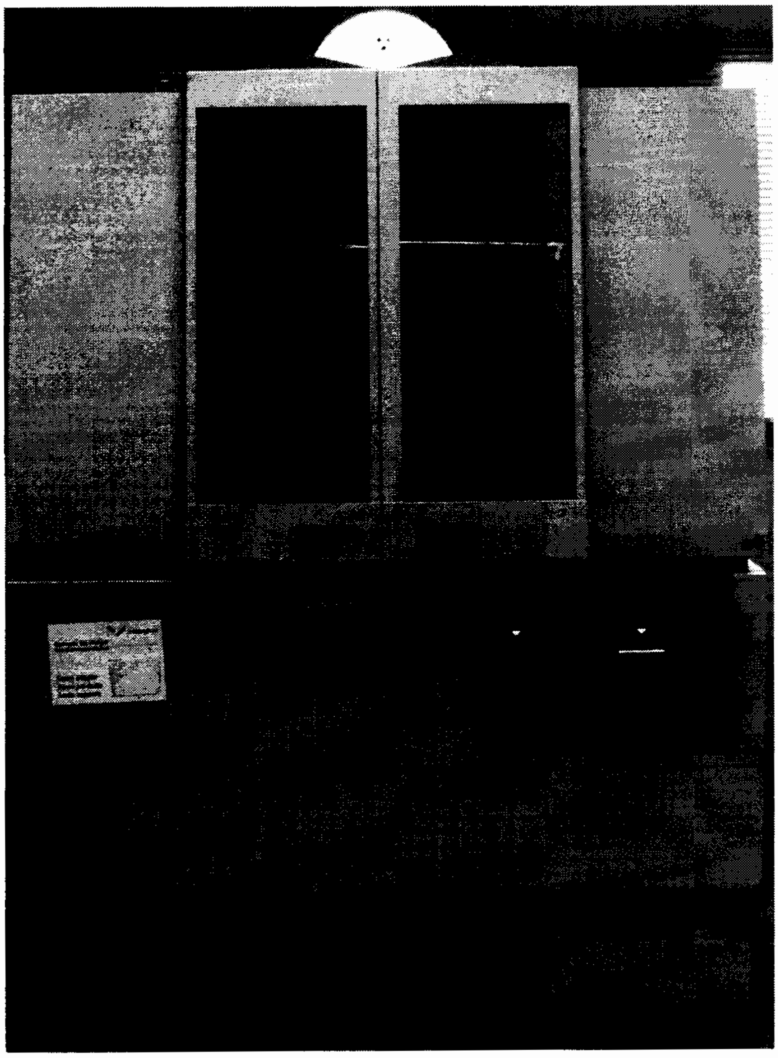

Figure 3.3 Philips X'Pert-MDP X-ray diffractometer used in this work

Lattice Parameter a

The diffraction of the incident waves through the crystal planes is illustrated in Figure 3.5. The distance d between crystal planes is given by Bragg's law [37, 38].

$$n\lambda = 2d \sin\theta \tag{3.2}$$

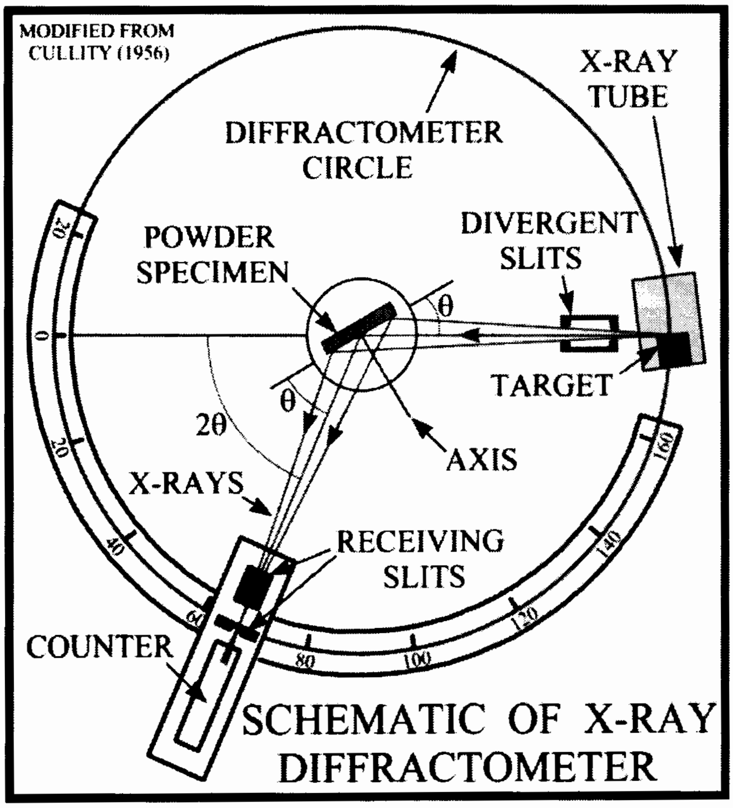

Figure 3.4 Schematic diagram of X-ray Diffractometer

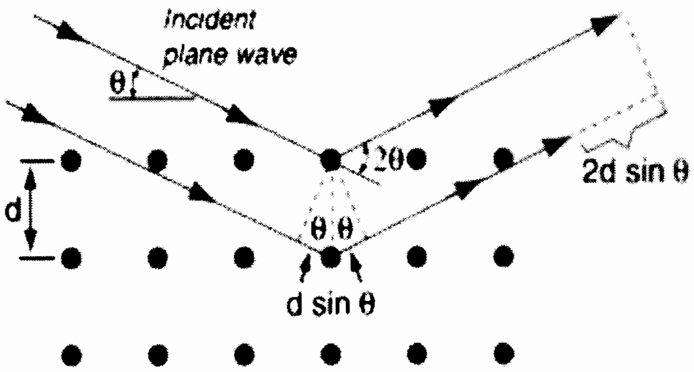

Figure 3.5 Bragg's law and diffraction through crystal planes

For cubic phases, each lattice parameter (a, b, c) can be determine using the Miller indices (hkl) of each reflection and the equation that follows [46]

$$a_o = d_{hkl}\sqrt{h^2 + k^2 + l^2} \tag{3.3}$$

Substituting Bragg's law gives

$$sin^2\theta = \frac{\lambda^2}{4a^2}(h^2 + k^2 + l^2) \tag{3.4}$$

The corresponding equation for a tetragonal crystal with axes a and c is given by

$$sin^2\theta = \frac{\lambda^2}{4}\left(\frac{h^2 + k^2}{a^2} + \frac{l^2}{c^2}\right) \tag{3.5}$$

The distance between crystal planes for a tetragonal crystal is given by

$$d_{hkl} = \frac{a}{\sqrt{h^2 + k^2 + (a^2/c^2)l^2}} \tag{3.6}$$

Scanning Electron Microscopy (SEM)

The surface morphology of the samples was characterized using a JEOL JSM-6010 LV Scanning Electron Microscopy (shown in Figure 3.6) operating at an acceleration voltage of 20 kV.

UV-Visible light Spectroscopy (UVS)

The optical band gap of the samples was determined from the UV absorption spectrum using a UV-2600 UV-VIS Spectrophotometer from SHIMADZU, as shown in Figure 3.7

The operating parameters are as follows: wavelength range (200 – 800 nm); SBW (2 nm) and data interval (1 nm). The spectra were recorded in absorbance mode versus wavelength.

The energy band gap E_g is determined by taking the cut off wavelength λ at the minimum value of the absorbance, using the following equation [52]:

$$E_g = \frac{hc}{e\lambda} \tag{3.7}$$

Where, Planck's constant h = 6.626×10^{-34} Js; speed of light c = 3.0×10^{8} m/s; electronic charge e = 1.6×10^{-19} C

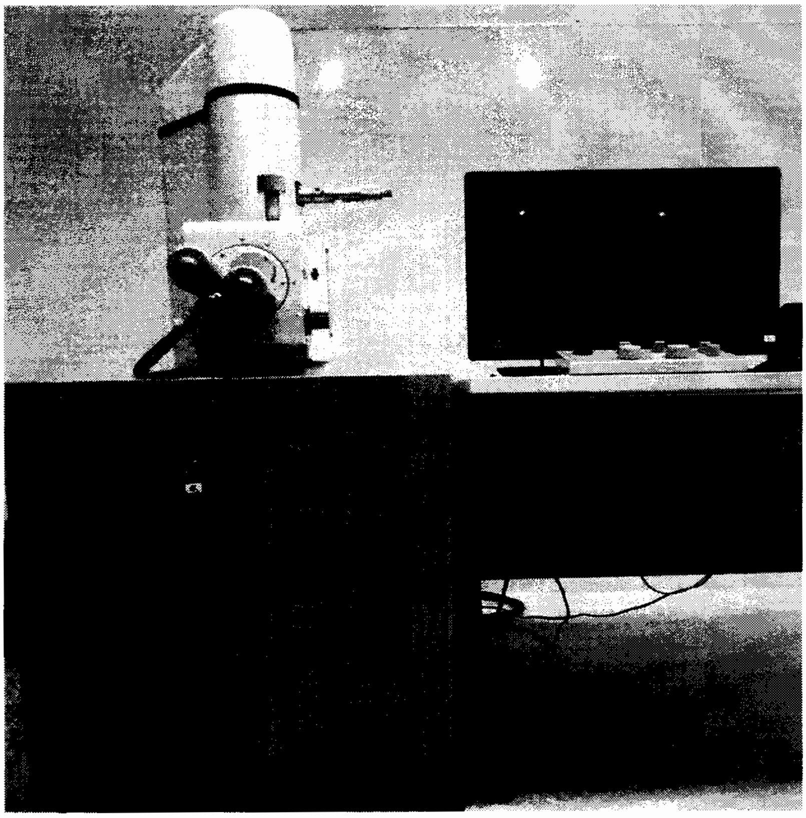

Figure 3.6 A JEOL JSM-6010LV Scanning Electron Microscopy

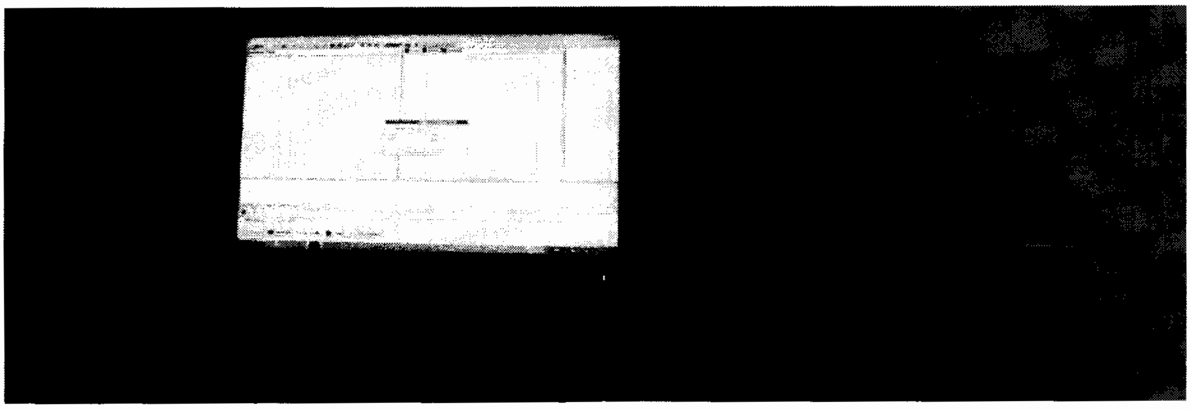

Figure 3.7 UV-2600 UV-VIS Spectrophotometer from SHIMADZU

Energy Dispersive X-ray Spectroscopy (EDX or EDS)

To investigate the elements present on the samples, EDX test was carried out. The EDX works on the principle that, when an incident electron or photon hits an unexcited atom, an inner shell electron is ejected, leaving a hole behind. An outer shell electron lowers its energy through the emission of an X-ray and moves to fill the hole. In this work an EDXRF model XGT-5200WR X-ray Analytical Microscope from HORIBA Scientific was used. See Figure 3.8

Figure 3.8 EDXRF (XGT-5200WR) X-ray Analytical Microscope from HORIBA

X-ray Photoelectron Spectroscopy (XPS)

XPS was used to determine the binding energy and elemental constituents present in the samples. Figure 3.9 shows the Thermo Al K- Alpha XPS machine (from South Korea) used for this research. XPS works on the photoelectric effect phenomenon. Low- energy X-rays are used to eject electrons from atoms. The binding energy E_B can be determined for an incident photon of frequency f, and ejected electron of energy E_e, using the following equation [38]:

$$E_B = hf - E_e \tag{3.8}$$

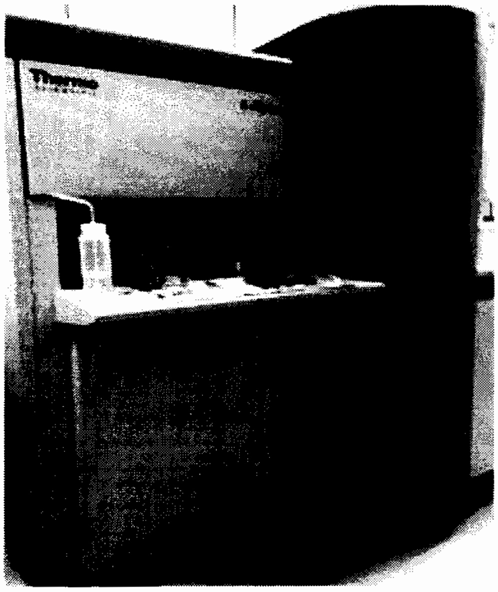

Figure 3.9 Thermo Al K- Alpha XPS machine (South Korea)

3.3 THE DYE-SENSITIZED SOLAR CELLS

The as prepared samples were immersed in a dye solution containing 0.0005 M of N3 dye for 24 hours. The samples are removed, ultrasonicated for 10 minutes and dried in an oven for 30 minutes at 80 °C. Platinum solution (H_2PtCl_6) to serve as the catalyst was coated on Fluorine-doped tin oxide (FTO) glass. The FTO glass was then dried in an oven for 30 minutes at 80 °C. is The platinum cathode was pressed on the TNT photoanode, and a KI/Iodine electrolyte injected in between to form a dye sensitized solar cell.

The effective area of the cell was set at about 0.2 cm^2. Light of intensity, 70 mW/cm^2 from a Xenon arc lamp was incident on the cell and the current-voltage characteristic measured using a Keithley 2400 source meter, shown in Figure 3.10. The performance of each solar cell was determined from the current-voltage characteristic by calculating the solar power conversion efficiency η using equations 2.5 and 2.6.

Figure 3.10 Computer, Keithley 2400 source meter, and Xenon arc lamp for I-V characterization of the solar cell

CHAPTER 4

RESULTS AND ANALYSIS

This chapter presents the experimental results of both undoped and Nitrogen - doped TiO_2 nanotubes. The samples were analyzed by SEM, XRD, UVS, EDX and XPS, and their efficiencies were tested in DSSCs.

4.1 SEM ANALYSIS

The SEM images of TNT doped with different concentrations of Nitrogenusing ammonia as source are displayed in Figure 4.1.

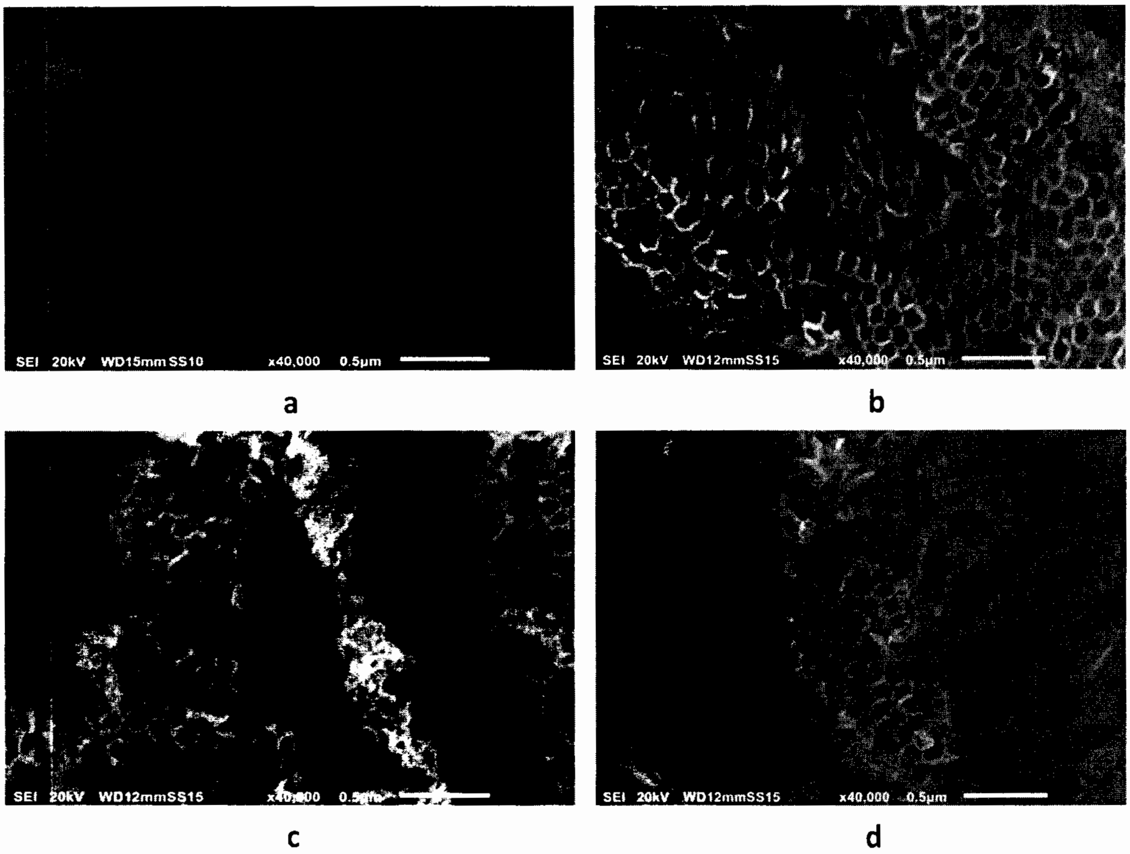

a b

c d

Figure 4.1 SEM images of TNT doped with different concentrations of Nitrogen using ammonia as source - (a) 1 %, (b) 3 %, (c) 6 % and (d) 12 %

The nanotubes are well-arrayed with an average diameter of about 100 nm and approximately 1.0 μm in length. The cross section of the nanotubes is roughlyhexagonal. It is observed that as dopant concentration increases, nanofibres begin to form and cover the surface of the nanotubes (Fig. 4.1 c, d).

Figure 4.2 displays the SEM images of Nitrogen–doped TNT calcinated at different temperatures. The average diameter of the nanotubes is observed to increase with calcination temperature from approximately 80 nm at 100 °C, to about 250 nm at 200 °C. Homogeneity of the nanotubes in Figure 4.2 is greater than in Figure 4.1.

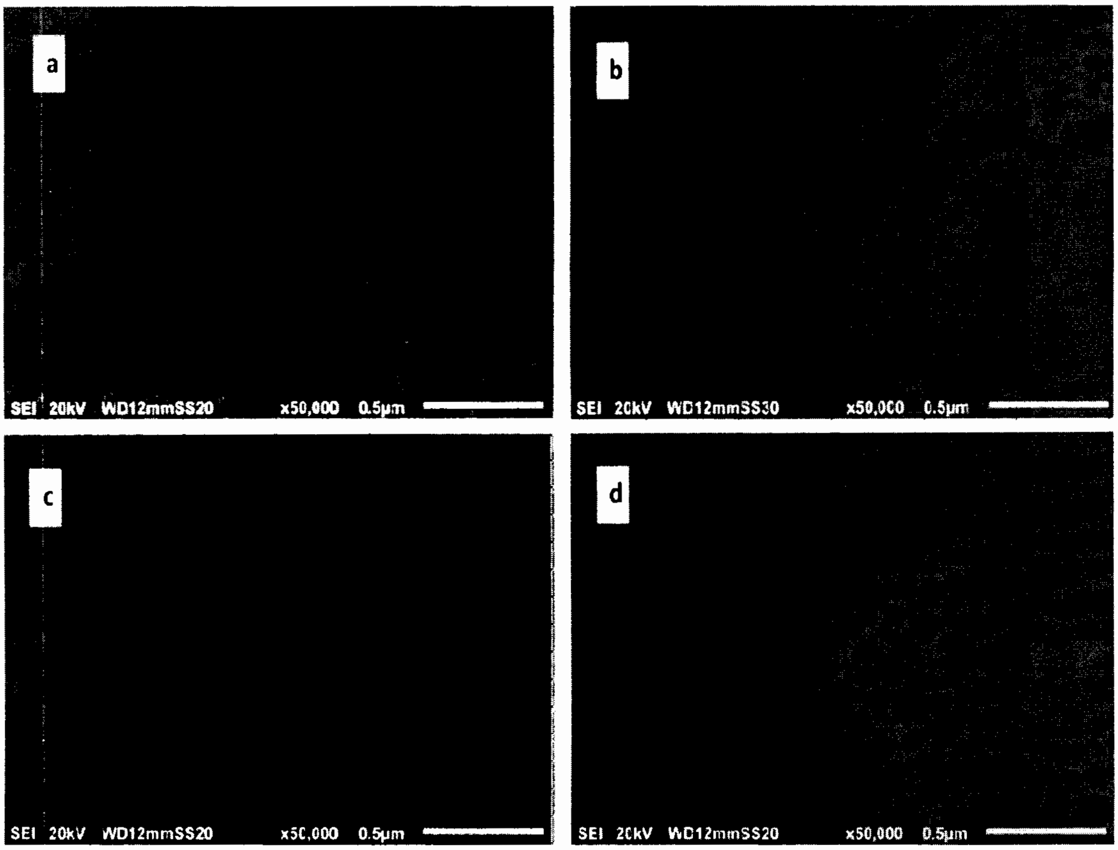

Figure 4.2 SEM images of N-doped TNT calcinated at different temperatures: (a) 100 °C, (b) 125 °C, (c) 150 °C and (d) 200 °C

When the anodization starts, bubbles are seen, and an oxide layer begins to form on the Ti sheet. TiO_2 nanotubes form on the oxide layer. Under the influence of the electric field, Ti^{4+}, OH^- and F^- ions diffuse through the electrolyte leading to the formation of a barrier layer. Dissolution of F^- ions result in formation of $[TiF_6]^{2-}$ ions.

Eventually, both the growth rate and dissolution rate reach equilibrium [53]. The formation of the nanotubes is summarized according to the following chemical equations [54, 55]:

$$2H_2O \rightarrow O_2 + 4e^- + 4H^+ \tag{4.1a}$$

$$Ti + O_2 \rightarrow TiO_2 \tag{4.1b}$$

$$TiO_2 + 6F^- + 4H^+ \rightarrow [TiF_6]^{2-} + 2H_2O \tag{4.1c}$$

4.2 XRD ANALYSIS

Figure 4.3 shows the XRD patterns of N-doped TNT with different amounts of ammonia. The Ti peaks at 38°, 40°, 53°, 70.6°, 76.2° and 77.5° can be ascribed to Titanium substrate. Their corresponding diffraction planes are (002), (101), (102), (103), (112) and (201), respectively. The A peaks at 25.5°, 35°, 37.5°, 48°, 54°, 55.3°, 62.7° and 75° may be assigned to TiO_2 anatase phase, and their respective corresponding diffractions are(101), (100), (103), (200), (105), (211), (204) and (215) [56, 57, 58]. The most prominent peak is the (101) anatase plane. For this plane, the average values of the crystallite size D, the distance between crystal planes d and the lattice parameters (a, b, c) were calculated to be D = 20.32 nm, d = 3.507 Å, a = b = 3.782 Å, c = 9.353 Å. These results are slightly different from those of pure TiO2 due to the doping effect of Nitrogen.

The XRD patterns of N-doped TNTcalcinated at different temperatures are displayed in Figure 4.4. The results reveal a predominant presence of the Ti peak at 2θ angles about 38°, 40°, 53°, 70.6°, 76.2° and 77.5°. These peaks can be assigned to the respective crystalline phases (002), (101), (102), (103), (112) and (201) [53, 58, 59]. The anatase phase patterns are observed at about 35° and 62.7°, which corresponds to the crystal planes (100) and (204) respectively. This indicates that low temperature crystalization of TiO_2 phases is possible [59]. However, calcination well below 450 °C resulted in low phase transformation [60, 61].

For the plane (204), the average values of the crystallite size D, the distance between crystal planes d and the lattice parameters (a, b, c) were calculated to be D = 27.08 nm, d = 1.482 Å, a = b = 3.780 Å, c = 9.545 Å. In comparison to pure TiO2, these values differ slightly but are in agreement with some reports.

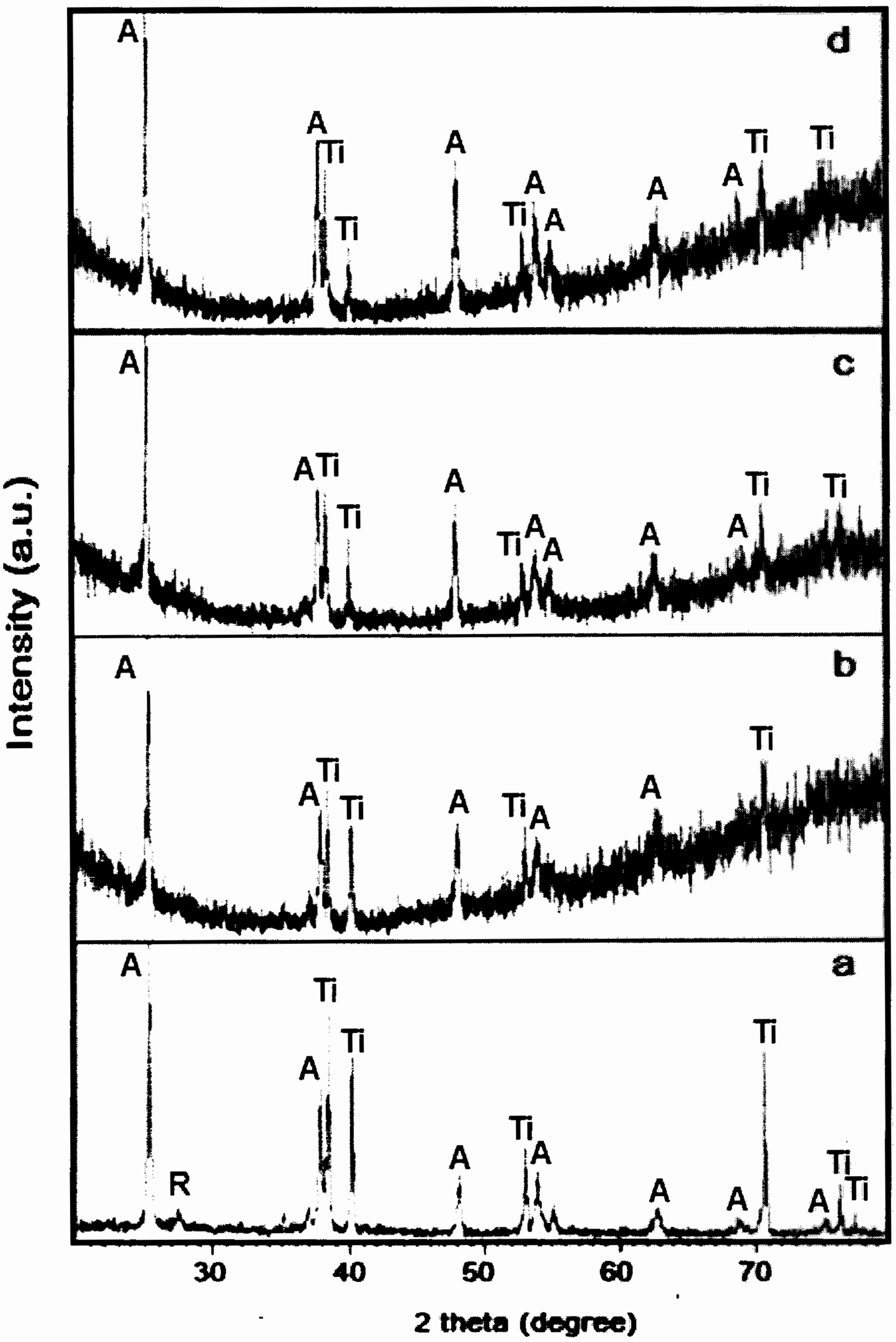

Figure 4.3 XRD patterns of N-doped TNT with different amounts of ammonia: (a) 1 %, (b) 3 %, (c)6 % and (d)12 %. [Ti = Titanium metal, A = anatase phase of TiO_2, R = rutile phase of TiO_2].

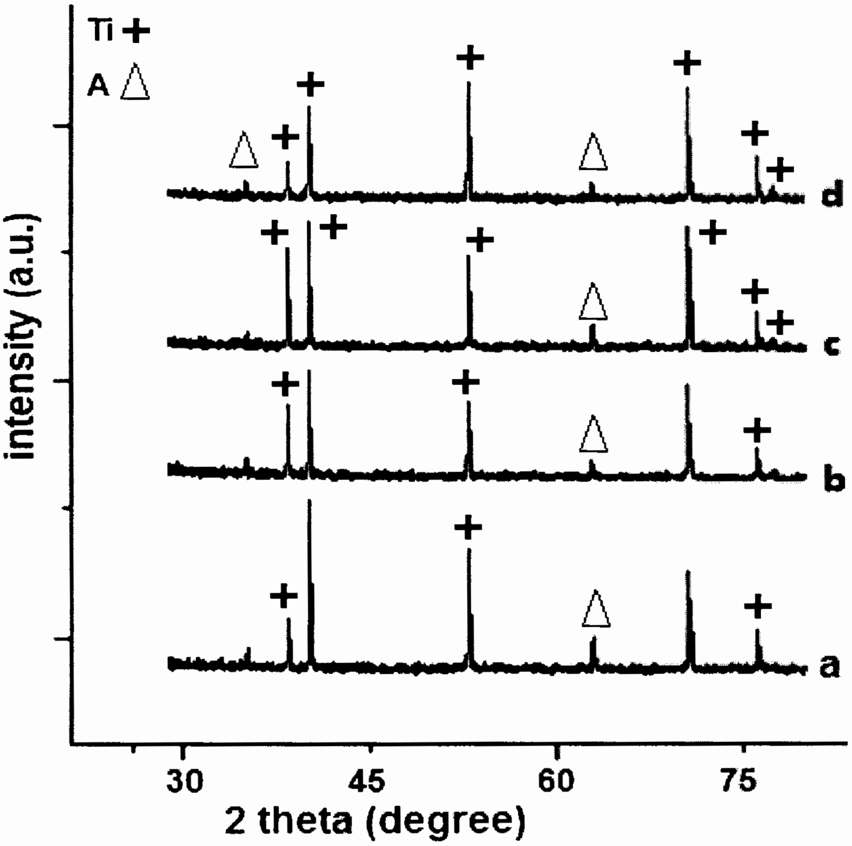

Figure 4.4 XRD patterns of N-doped TNT calcinated at different temperatures: (a) 100 °C, (b) 125 °C, (c) 150 °C and (d) 200 °C. [+ = Titanium metal, Δ = anatase phase of TiO_2].

4.3 UV – VISIBLE LIGHT SPECTRA ANALYSIS

The optical response of the N-doped TiO_2 nanotubes is shown in Figure 4.5. Notice that as the amount of dopant increases, the absorption edge shifts from shorter wavelengths to longer wavelengths. The optical band gap was calculated using equation 3.6. Table 4.1 shows that the absorption edge red-shifts from 394 nm to 435 nm as the amount of NH_3 is increased from 1 % vol to 12 % vol respectively. The corresponding band gap energies reduce from 3.15 eV to 2.85 eV. The reduction in optical band gap with increasing dopant concentration is in agreement with the works of S. Zhou et al and R. Dholam et al [4, 62]. The band gap of 3.15 eV for the 1% vol N-doped TNT is very close to that of pure TiO_2 in anatase phase, which is 3.2 eV [33, 43].

The reduction in optical band gap can be ascribed to several reasons. It could be that upon doping, the oxygen atoms in the TiO_2 lattice are substituted by N atoms [47] leading to the formation of a narrow N_{2p} band above the top of the O_{2p} valence band. [62]. Hence, electron excitation by UV light in the doped samples can occur in both the valence band and the narrow band, whereas, excitation can occur only in the valence band for pure TiO_2 [63]. In addition, presence of the narrow band or mid-band will facilitate electron transition into the conduction band for the doped samples [64].

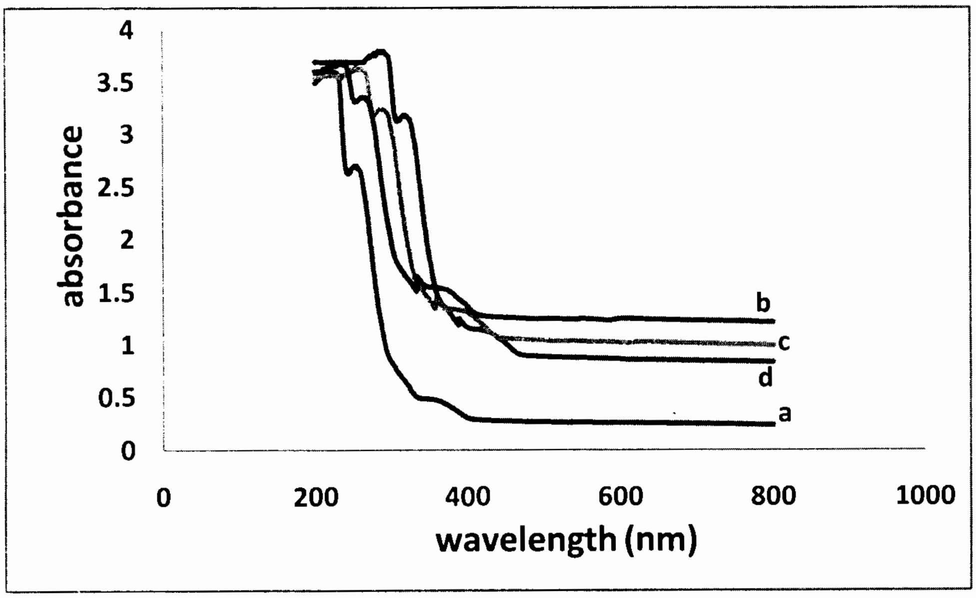

Figure 4.5 UV-Vis spectrum of N-doped TNT with different amounts of ammonia: (a) 1 %, (b) 3 %, (c)6 % and (d)12 %

In Figure 4.6 the absorption edge of N-doped TNT is observed to change when the calcination temperature changes. There is a general shift towards the visible region from a wavelength of 359 nm for the sample calcinated at 100 °C, to 415 nm for the sample calcinated at 125 °C. As seen in Table 4.2, the calculated optical band gap energy first decreases with calcination temperature, from 3.46 eV (at 100 °C), to 2.99 eV (at 125 °C). But, at higher temperatures, the band gap increases to 3.27 eV (at 150 °C) and to 3.35 eV (at 200 °C). These results are in accord with the reports of references [10, 11, 65]. The band gap reduction as temperature increases from 100 °C to 125 °C can be attributed to the transformation of amorphous TiO_2 into crystalline anatase phase [18, 56].

Further increase in calcination temperature may in turn reduce the amount of Nitrogen atoms that effectively get doped into the TiO_2 lattice [10]. It is possible that at higher temperatures, the doped Nitrogen can introduce new energy states just below the bottom of the conduction band. These new states may serve as recombination sites for electron-hole pairs.

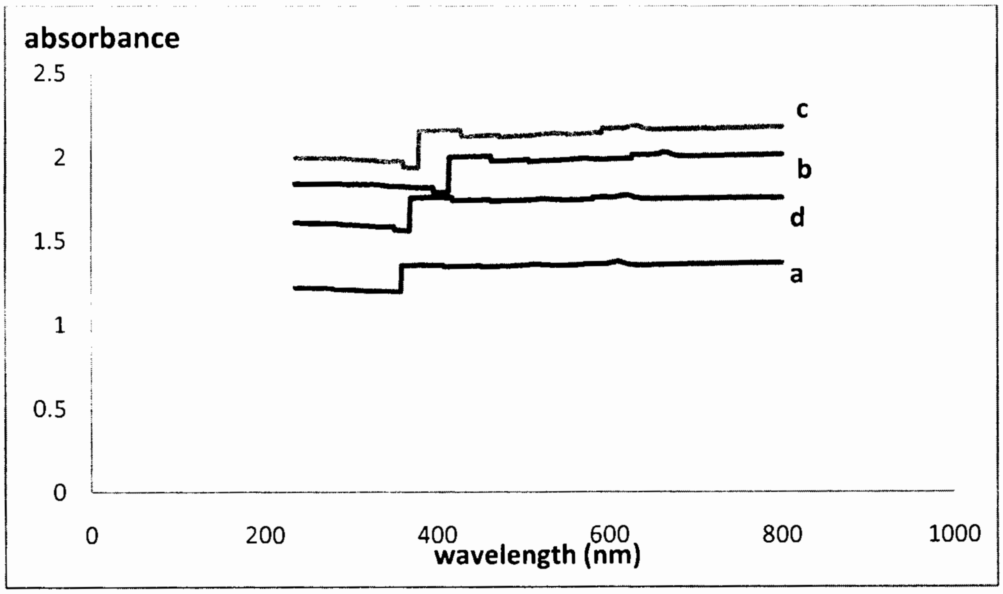

Figure 4.6 **UV-Vis spectrum of N-doped TNT calcinated at different temperatures: (a) 100 °C, (b) 125 °C, (c) 150 °C and (d) 200 °C**

Table 4.1 Optical band gap of N-doped TNT with different amounts of ammonia

	1% vol NH_3	**3% vol NH_3**	**6% vol NH_3**	**12% vol NH_3**
Absorption edge wavelength λ (nm)	394	404	417	435
Optical band gap E (eV)	3.15	3.08	2.98	2.85

Table 4.2 Optical band gap of N-doped TNT calcinated at different temperatures

	100 °C	**125 °C**	**150 °C**	**200 °C**
Absorption edge wavelength λ (nm)	359	415	380	371
Optical band gapE (eV)	3.46	2.99	3.27	3.35

4.4 EDX ANALYSIS

Figure 4.7 and Figure 4.8 show the EDX spectra of N-doped TNTs. In Figure 4.7 the dopant concentration is varied whereas in Figure 4.8, the calcination temperature is changed while keeping the dopant amount constant. The element Ti was found in the EDX spectra of all the samples. This indicates the successful formation of TiO_2 nanotubes on the surface of the titanium sheets [62], as confirmed by the SEM images in Figure 4.1 and Figure 4.2.

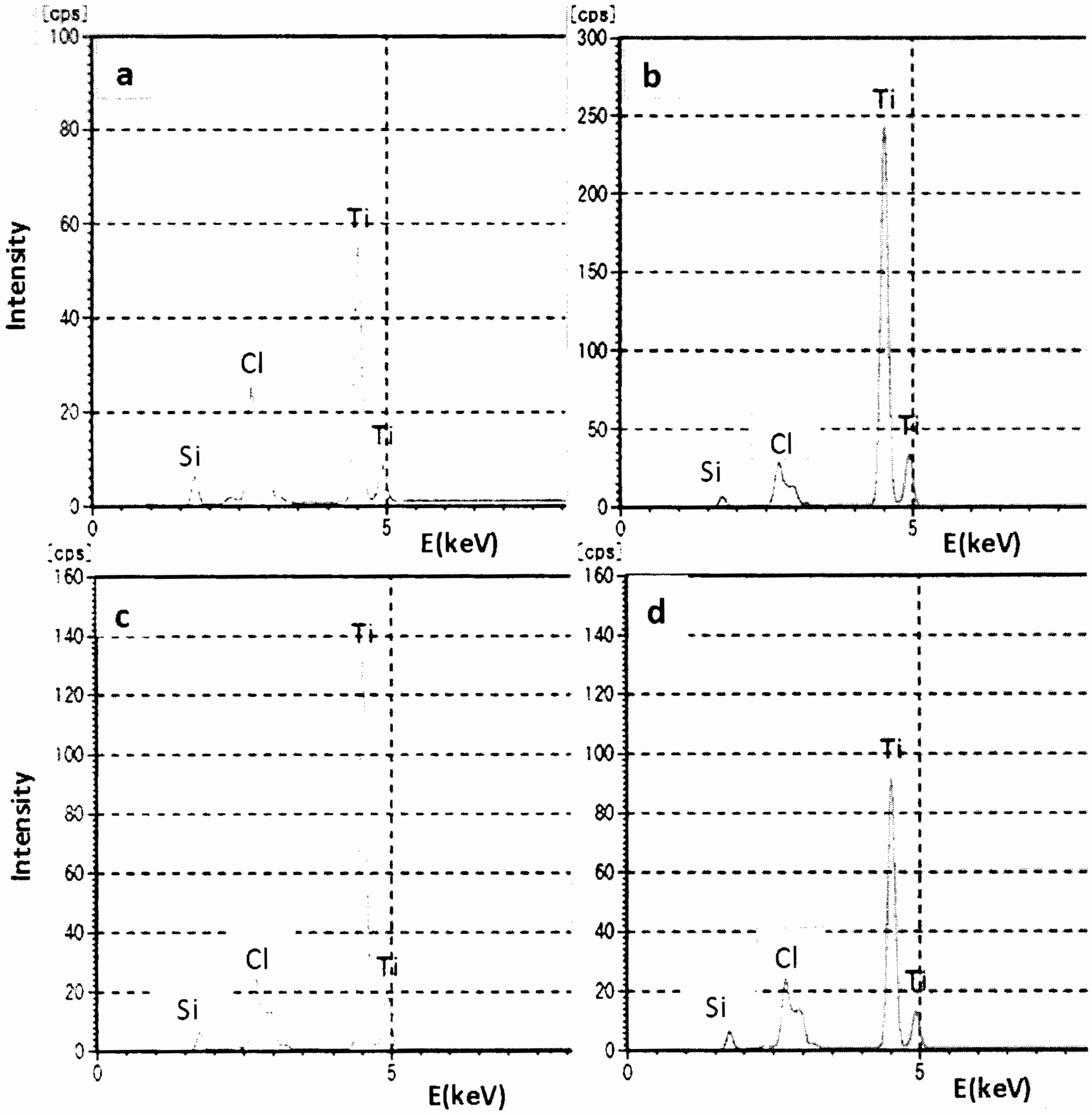

Figure 4.7 EDS spectra of N-doped TNT with different amounts of ammonia: - (a) 1 %, (b) 3 %, (c) 6 % and (d) 12 %

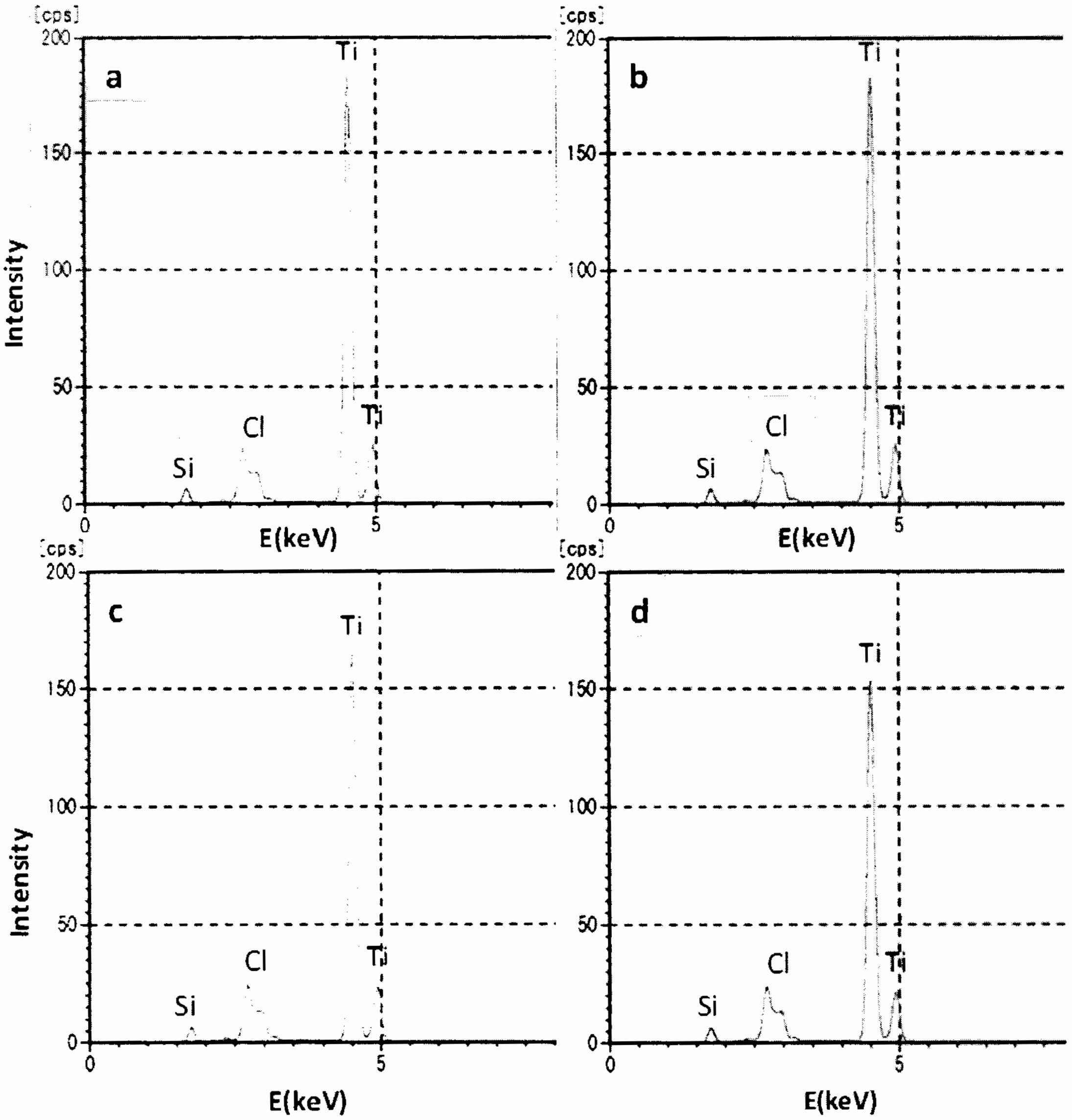

Figure 4.8 EDS spectra of N-doped TNT calcinated at different temperatures: (a) 100 °C, (b) 125 °C, (c) 150 °C and (d) 200 °C

4.5 XPS ANALYSIS

X-ray photoelectron spectroscopy (XPS) was used to examine the chemical composition of the prepared samples. Figure 4.9 shows the XPS spectra of N-doped TNT with different dopant amounts of ammonia. Figure 4.10 displays the C_{1s}, O_{1s}, N_{1s}, and Ti_{2p} spectra peaks N-TNT with 6 vol % of ammonia. Figure 4.11 and Figure 4.12 show the XPS spectra of N-doped TNT at different calcination temperatures.

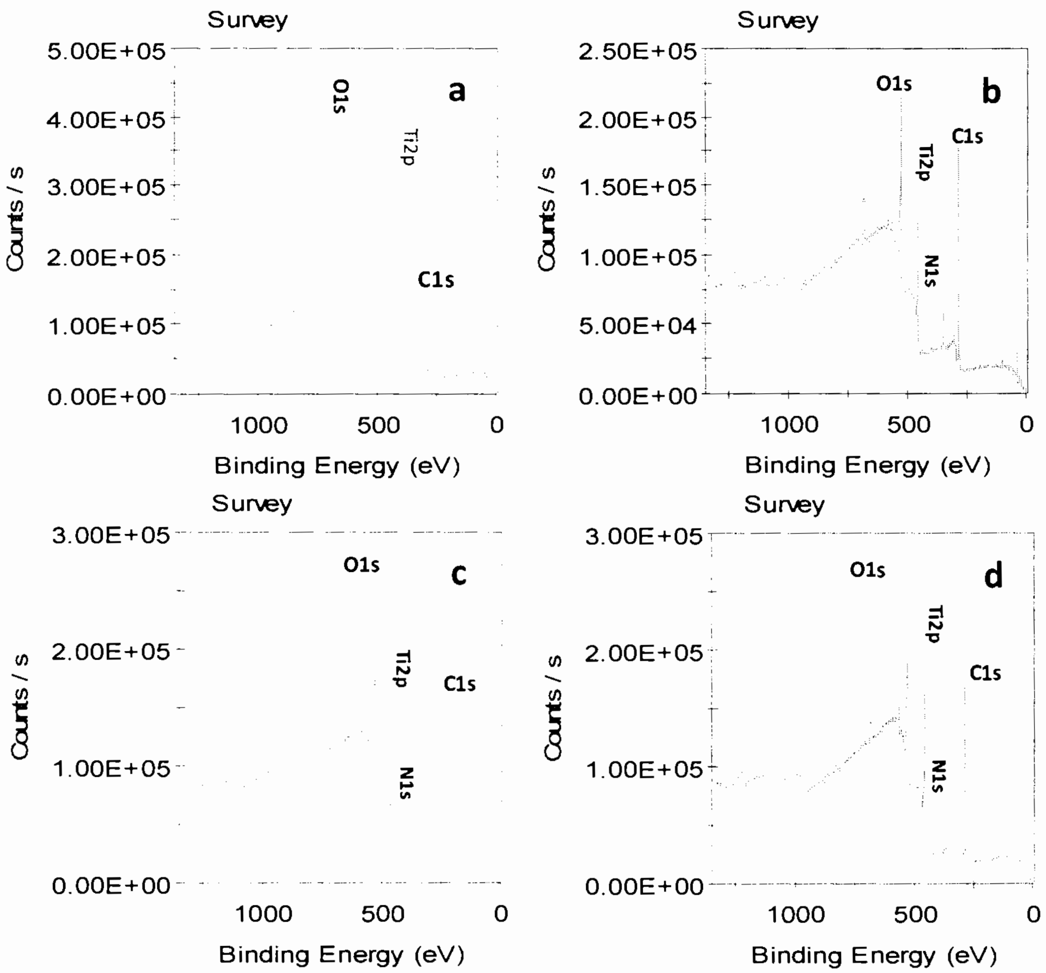

Figure 4.9 XPS spectra of N-doped TNT with ammonia (a) 1 %, (b) 3 %, (c) 6 %, (d) 12 %

In Figure 4.10, the XPS spectra of N-doped TNT with 6 % vol of ammonia are displayed. The C_{1s} peak that appears at 284.1 eV can be due to pollution of hydrocarbon from the XPS instrument [10, 62]. The XPS spectrum of O_{1s} shows a peak at 529.5 eV which can be attributed to the Ti-O bond [65].

The Ti_{2p} XPS spectrum shows two peaks – one at 458.1 eV and the other at 463.9 eV. The 458.1 eV peak corresponds to the Ti_{2p} (1/2) electron binding energy, while the 463.9 eV peak corresponds to the Ti_{2p} (3/2) electron binding energy. Both peaks indicate that Ti is present in the Ti^{4+} oxidation state [66, 67]. For pure TiO_2, the Ti_{2p} characteristic peaks are positioned at 458.5 eV and 464.2 eV, which indicates a small shift when compared to the N-doped samples. This could be accounted for by the substitution of oxygen atoms by nitrogen atoms, resulting in the formation of O-Ti-N bonds and changing the Ti electron binding energy [62].

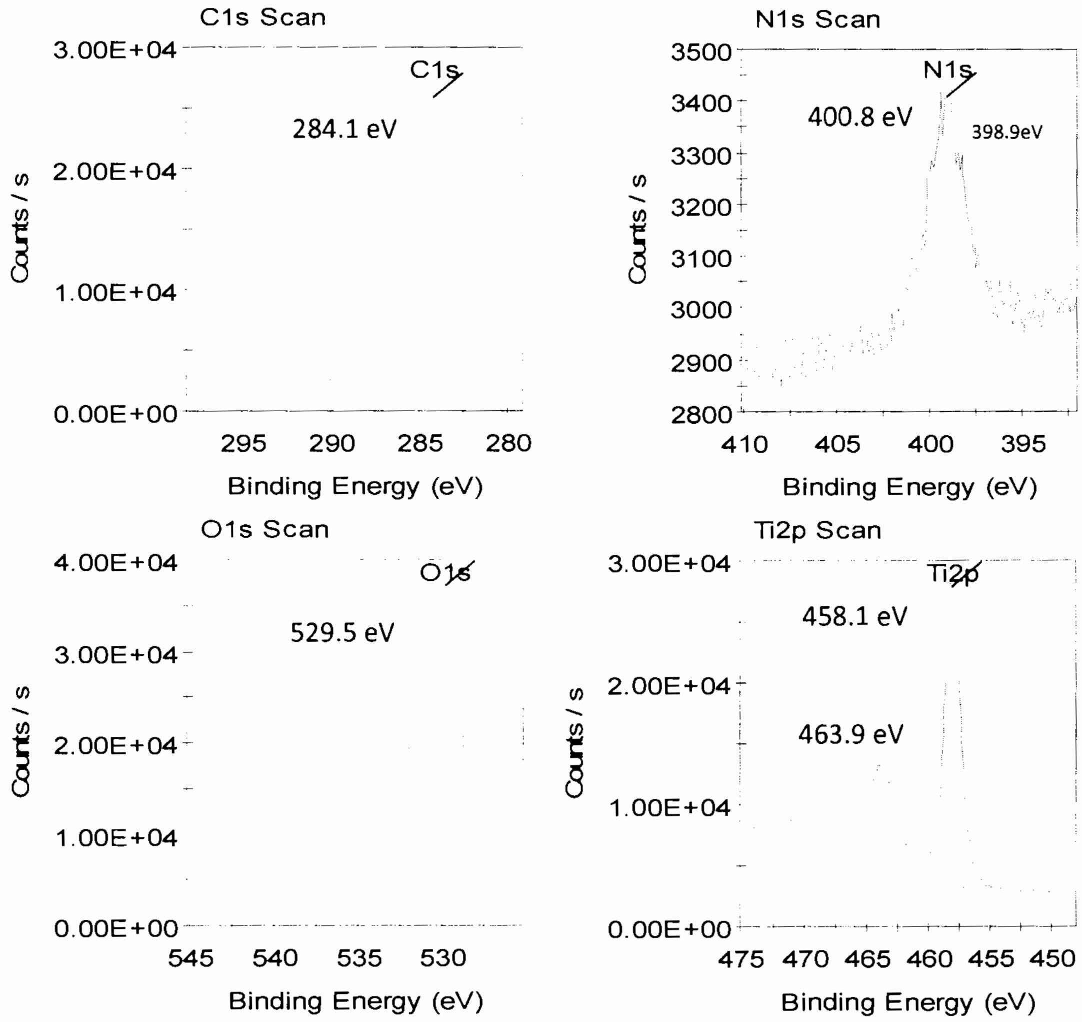

Figure 4.10 High resolution XPS spectra of N-doped TNT with 6 % of ammonia

The N_{1s} XPS spectrum reveals the peaks located at 398.9 eV, and 400.8 eV. The 398.9 eV peak can be attributed to the substitutional Ti-N nitride bond [25]. The N_{1s} 400.8 eV peak can be assigned to the Ti-N-O bonds. The absence of a peak around 402.2, which is due to oxides or hydrides of Nitrogen, suggests the absence of interstitial N bonds [28].

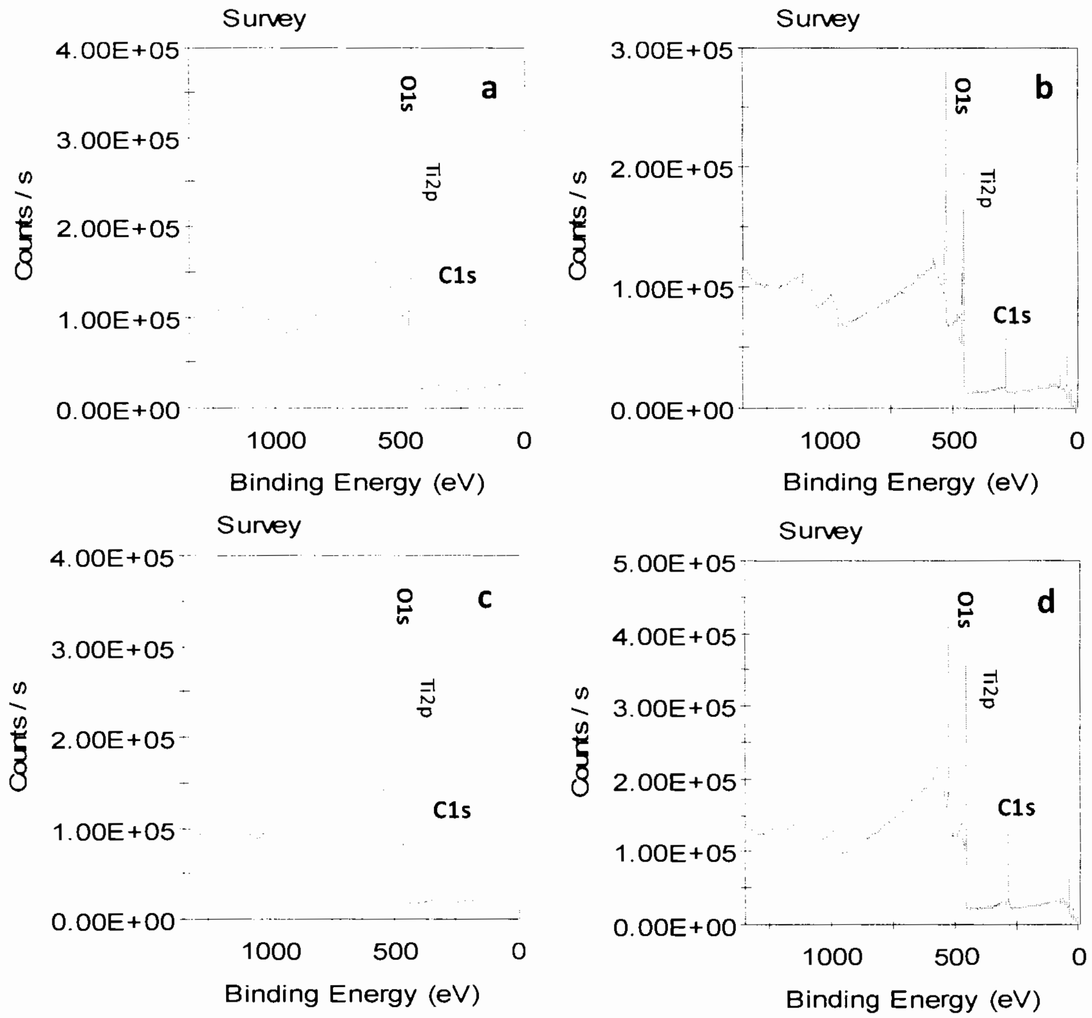

Figure 4.11 XPS spectra of N-TNT calcinated at different temperatures: (a) 100 °C, (b) 125 °C, (c) 150 °C, (d) 200 °C

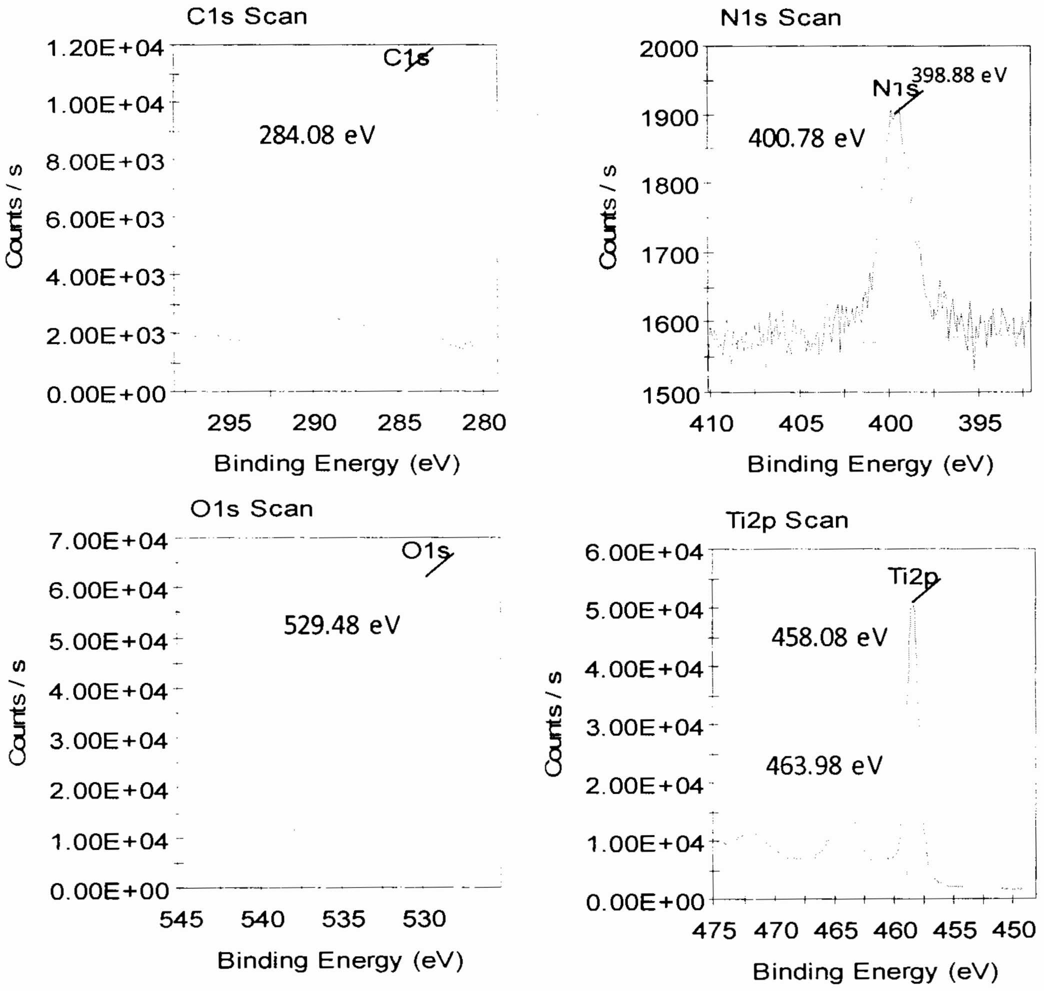

Figure 4.12 XPS spectra of N-doped TNT calcinated at 125 °C

The atomic percentages of elements in the as-prepared samples are shown in Table 4.3 and Table 4.4. In Set 1, the effective N-doping is observed to increase as the amount of ammonia increases. However, in Set 2, the effective N-doping decreases as the calcination temperature increases.

Table 4.3 Atomic percentages of elements in the N-doped TNT with different amounts of ammonia: Set 1

Peaks	1 % vol NH_3	3 % vol NH_3	6 % vol NH_3	12 % vol NH_3
Ti2p (%)	10.2544	7.8168	11.2034	10.0994
O1s (%)	32.7501	26.3207	33.2726	31.6875
N1s (%)	0.44525	0.78506	1.05442	1.36971
C1s (%)	56.5502	65.0774	54.4696	56.8434

Table 4.4 Atomic percentages of elements in the N-doped TNT at different calcination temperatures: Set 2

Peaks	100 °C	125 °C	150 °C	200 °C
Ti2p (%)	18.1561	21.0293	20.2241	21.4037
O1s (%)	46.1314	51.8307	49.4829	49.491
N1s (%)	0.980323	0.977498	0.912169	0.703894
C1s (%)	34.7322	26.1625	29.3808	28.4014

We note that the XPS analysis provides a more detail chemical composition of the sample surfaces, than the EDX analysis. In addition,XPStest can give the percentages of the elements present.

4.6 PERFORMANCE IN DYE-SENSITIZED SOLAR CELLS

The performance of the as-prepared samples was tested in DSSCs. The current-voltage characteristics are displayed in Figure 4.13 and Figure 4.14. The conversion efficiencies are shown in Table 4.5 and Table 4.6. As observed in Table 4.5, the power conversion efficiency of the doped samples increases with increase in dopant amount. This is in agreement with the results of references [68 - 70]. A maximum efficiency of 7.98 % was obtained for the sample doped with 6 % vol of ammonia. At 12 % vol of ammonia, the efficiency of the DSSC is found to be less than that with 6 % vol of ammonia. This indicates that there is a critical dopant concentration, above which the efficiency starts to decrease. This is also in accordance with the references [71 - 75].

Increase in efficiency for ammonia 1 vol % to 6 % vol of ammonia could be due to optical band gap reduction as Nitrogen incorporates into the TNT [76]. The low efficiency for the N-TNT with 12 % vol of ammonia could be due to several reasons. For one, too much ammonia may cause many oxygen vacancies in the TiO_2 lattice. These vacancies would serve as recombination centers for the charge carriers (electrons and holes). As a result, there is a decrease in the conversion efficiency [10]. Furthermore, as seen from the SEM image in Figure 4.1d, nanofibres or "nanograss" and particles begin to form and cover the surface of the nanotubes with high amounts of ammonia. This leads to inhomogeneity which in turn reduces the power conversion efficiency of the cell [77].

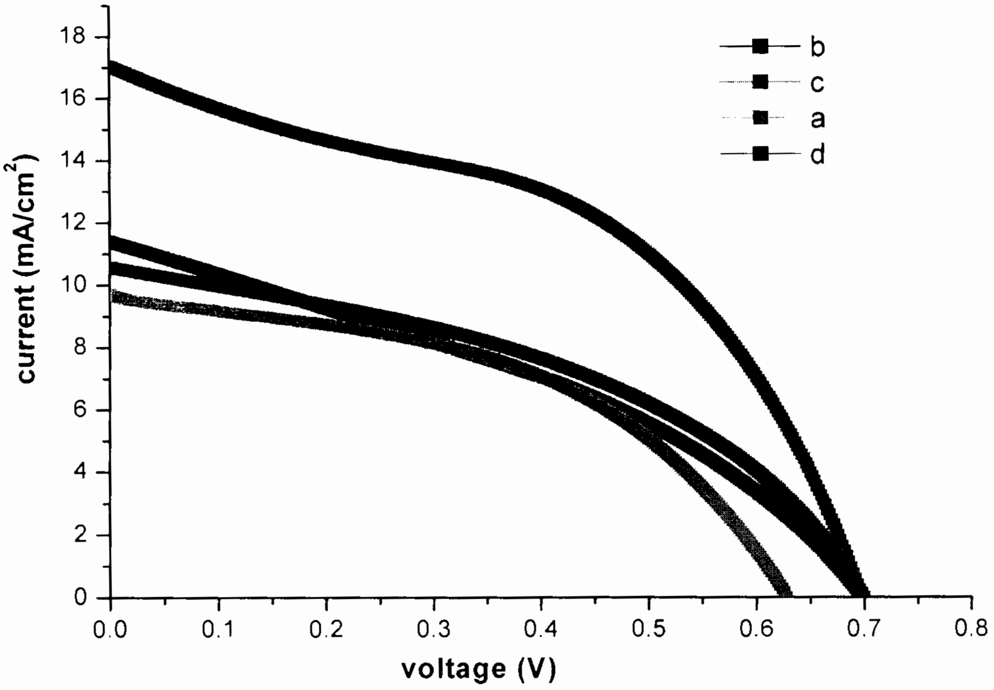

Figure 4.13 Current-Voltage curves of DSSCs with TNT doped with different amounts of Nitrogen using ammonia as source - (a) 1 %, (b) 3 %, (c) 6 % and (d) 12 %

Table 4.5 Efficiencies of DSSCs with N-doped TNT with different amounts of ammonia

Amount of NH_3	V_{OC} (volts)	I_{SC} (mA/cm^2)	V_M (volts)	I_M (mA/cm^2)	FF	η (%)
1 %	0.63	09.71	0.42	6.76	0.46	4.01
3 %	0.69	11.40	0.44	6.53	0.37	4.16
6 %	0.70	17.00	0.47	11.77	0.47	7.98
12 %	0.70	10.56	0.46	6.84	0.43	4.54

Table 4.6 shows that the conversion efficiency first increases with calcination temperature [10, 11, 78] and reaches 4.61 % at 125 °C. However, for higher calcination temperatures - 150 °C and 200 °C, the efficiency is observed to decrease [11]. A number of reasons could account for these outcomes. Improved crystallinity at 125 °C may be responsible for higher photocatalytic activity over the sample calcinated at 100 °C [79]. As the calcination temperature increases to 150 °C and 200 °C, it could result in decrease in the effective amount of Nitrogen doped into the samples [10]. As a consequence, the photocatalytic activity and efficiency reduces for higher calcination temperatures.

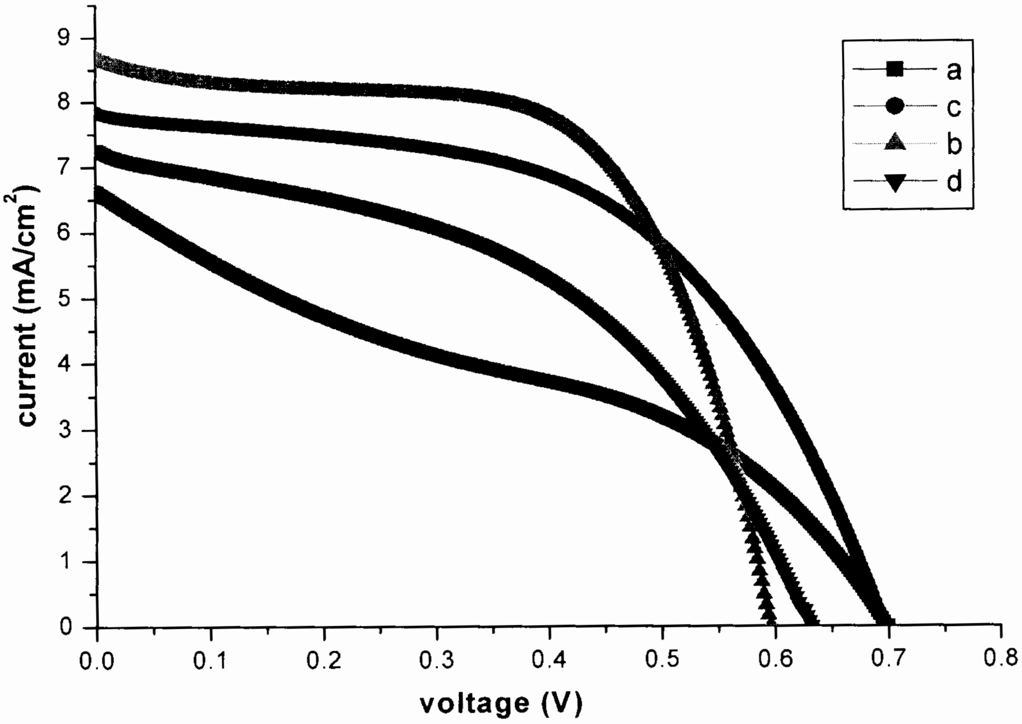

Figure 4.14 Current-Voltage curves of DSSCs with N-doped TNT calcinated at different temperatures: (a) 100 °C, (b) 125 °C, (c) 150 °C and (d) 200 °C

Table 4.6 Efficiencies of DSSCs with N-doped TNT calcinated at different temperatures

Calcination Temperature	V_{OC} (volts)	I_{SC} (mA/cm^2)	V_M (volts)	I_M (mA/cm^2)	FF	η (%)
100°C	0.70	6.64	0.48	3.33	0.34	2.26
125°C	0.60	8.68	0.44	7.30	0.62	4.61
150°C	0.63	7.28	0.48	6.08	0.64	4.20
200°C	0.69	7.85	0.41	5.16	0.39	3.01

The incident photon-to-current conversion efficiency IPCE for each cell as shown in Table 4.7, were calculated using equation 2.4 at wavelength 500 nm. The maximum IPCE = 54.8 %, was obtained for the DSSC with NH_3 6 % in Set 1.

Table 4.7 Incident photon-to-current conversion efficiency IPCE of the DSSCs

	Set 1				Set 2			
Variables	NH_3 1 %	NH_3 3 %	NH_3 6 %	NH_3 12 %	100°C	125°C	150°C	200°C
IPCE (%)	31.3	36.7	54.8	34.1	21.4	28.0	23.5	25.3

It can be observed that the samples in Set 1 prepared by varying the amount of ammonia had overall power conversion efficiencies greater than those in Set 2 prepared by varying the calcination temperature. The reason for this could be that the samples in Set 1 were all annealed at a much higher temperature of 500°C, whereas Set 2 samples were calcined to at most 200°C. Such high temperatures enhanced the transformation of amorphous TiO_2 into anatase [80, 81]. XRD results in Figure 4.3 and Figure 4.4 Set 1 confirm the strong presence of anatase phases in Set 1 over Set 2 samples. Furthermore, pre-calcination (before doping) in Set 1 samples might result in higher current densities over post-calcination (after doping) in Set 2 samples. Also, high temperature aging in Set 2 may lead to more surface deposition of Nitrogen and hydrides, giving rise to high electronic resistance on the samples [82].

CHAPTER 5

CONCLUSION AND RECOMMENDATIONS

5.1 SUMMARY OF RESULTS

TiO_2 nanotubes have been synthesized by DC Anodization at 50V for 2 hours in an electrolyte solution of ethylene glycol (EG), ammonium fluoride (0.3 wt % NH_4F) and deionized water (2 vol % H_2O). Two sets of N-doped TiO_2 nanotubes were prepared using 1M ammonia (NH_3) solution as Nitrogen source. In Set 1, after calcination at 500 °C, the TNTs were aged in a solution with different amounts of ammonia (1 %, 3 %, 6 % and 12 %). Meanwhile in Set 2, the TNTs were first doped with 5 % vol ammonia and then calcinated at different temperatures (100 °C, 125 °C, 150 °C and 200 °C).The samples were analyzed by SEM, XRD, UVS, EDX, and XPS. The performance of each sample was tested in a dye-sensitized solar cell (DSSC). The results of characterization and performance test in DSSCs can be summarized as follows:

SEM images confirm the successful formation of TiO_2 nanotubes with an average diameter of 100 nm for Set 1 samples. But the average tube diameter increased significantly from about 80 nm to about 250 nm for Set 2 samples, as the calcination temperature was increased from 100 °C to 200 °C.

XRD patterns showed a higher presence of the anatase phase when the amount of ammonia was varied, than when calcination temperature was varied. This could be because the latter was calcinated at a much higher temperature of 500 °C prior to doping. The maximum calcination temperature of 200 °C in the former is too low for complete phase transformation. The average crystallite size D and the distance between crystal planes d for the anatase plane (101) were D = 20.32 nm, d = 3.507 Å in Set 1. For the plane (204) in Set 2, D = 27.08 nm, d = 1.482 Å.

The presence of Ti in the EDX spectra of all the samples indicates the successful formation of TiO_2 nanotubes on the surface of the titanium sheets.

XPS results also confirm the presence of Nitrogen in the samples. In Set 1, the percentage of Nitrogen was found to increase as the amount of ammonia was increased. On the contrary, in Set 2, the percentage of Nitrogen was found to decrease as the calcination temperature was increased. This implies that increase in calcination temperature in turn reduces the amount of Nitrogen that effectively dopes into the TiO_2 lattice. For the sample with 6 % vol of ammonia, the Ti_{2p} peaks at 458.1 eV and 463.9 eV could be due to substitution of oxygen atoms by nitrogen atoms, resulting in the formation of O-Ti-N bonds. The N_{1s} peak at 400.8 eV can be assigned to the Ti-N-O bonds. These strongly support the successful doping of Nitrogen into the TiO_2 lattice. And that the N-doping is substitutional rather than interstitial.

UVS analysis showed that for Set 1, the optical band gap reduced with increase in the amount of ammonia, from 3.15 eV (at 1 % vol NH_3) to 2.85 eV (at 12 % vol NH_3). This could be due to increase in percentage of the Nitrogen and the formation of mid band gaps. A band gap of 2.85 eV corresponds to a red shift in light absorption into the visible region with wavelength 435 nm. In Set 2, the band gap reduced from 3.46 eV (at 100 °C) to 2.99 eV (at 125 °C), and increased with further increase in calcination temperature. The reduction in band gap at the beginning is due to improved crystallization. Later on, as calcination temperature increases, the amount of Nitrogen that effectively dopes into the TiO_2 lattice reduces. This is confirmed by the XPS results in Table 4.4. As a result the band gap increases. A band gap of 2.99 eV corresponds to a red shift in light absorption into the visible region with wavelength 415 nm.

In Set 1, the DSSC with 6 % vol NH_3 had the maximum efficiency of 7.89 %. Further increase in Nitrogen doping leads to formation of cracks, inhomogeneity, and recombination sites, and hence decrease in efficiency [83]. Meanwhile in Set 2, the maximum efficiency of 4.62 % was obtained for the sample calcinated at 125°C. This can be explained in a similar way as attributed to band gap variation. The 7.89 % efficiency in Set 1 corresponds to approximately 50 % efficiency improvement, while the 4.62 % efficiency in Set 2 corresponds to approximately 42 % efficiency improvement. The DSSC with NH_3 6 % in Set 1 had the maximum IPCE of 54.8 %. So Set 1 shows better results over Set 2. This could be due to better crystallization and phase transformation in Set 1 as a result of higher calcination temperature. High photocurrent implies more photo-induced charges, which lowers recombination of electron-hole pairs. In addition, lager crystallite size in Set 2 means larger surface area to volume ratio, hence, reduced photocatalytic activity [84]. Also, it could be due to the slight differences in the method of synthesis.

5.2 RECOMMENDATIONS

The obtained efficiencies for the two sets of data can be improved in several ways. During the anodization process, parameters such as anodizing temperature, applied voltage, composition, pH and concentration of electrolyte, and anodizing time, could be controlled or adjusted to influence the growth, size and orderliness of nanotubes [85, 86]. For future development of this research work and improvement of optical and photocatalytic properties of TiO_2 nanotubes, it is recommended to investigate the influence of the following factors: type of doping element, dopant source, method of synthesis of the TNTs and the DSSCs. The optimum dopant concentration and calcination temperature will vary depending on method of preparation and source of dopant.

REFERENCES

REFERENCES

[1] O'Regan B, Grätzel M. "A low-cost, high-efficiency solar cell based on dye sensitized colloidal TiO_2 films", **Nature**. 353: 737–739, 1991.

[2] Yanyan Zhang, et al. "Synthesis and characterization of TiO_2 nanotube for humidity sensing", **Applied Surface Science**. 254: 5545-5547, 2008.

[3] J.H. Park, S. Kim, A.J. Bard. "Novel carbon-doped TiO_2 nanotube arrays with high aspect rations for efficient solar water splitting", **Nano Letters**. 6: 24-28, 2006.

[4] R. Dholan, N. Patel, M. Adami, A. Miotello. "Hydrogen production by photocatalytic water-splitting using Cr- or Fe-doped TiO_2 composite thin films photocatalysts", **International Journal of Hydrogen Energy**. 34(13): 1-10, 2009.

[5] N. Kilinc, E. Sennik and Z.Z. Ozturk. "Fabrication of TiO_2 nanotubes by anodization of Ti thin films for VOC sensing", **Thin Solid Films**. 520: 953-958, 2011.

[6] E. Arpac, et al. "Photocatalytic performance of Sn-doped and undoped TiO_2 nanostructured thin films under UV and vis-lights", **Journal of Hazardous Materials**. 140: 69-74, 2007.

[7] Clemens Burda, Yongbing Lou, et al. "Enhanced Nitrogen-doping in TiO_2 nanoparticles", **Nano Letters**. 3(8): 1049-1051, 2003.

[8] Doohun Kim and et al. "Bamboo-type TiO_2 nanotubes: Improved Conversion Efficiency in Dye-sensitized solar cells", **J.AM.CHEM.SOC**. 130: 16454-16455, 2008.

[9] Shiqi Li, et al. "The role of the TiO_2 nanotubes array morphologies in the dye-sensitized solar cells", **Thin Solid Films**. 520: 689-693, 2011.

[10] Jiaqing Geng, et al. "Nitrogen-doped TiO_2 nanotubes with enhanced photocatalytic activity synthesized by a facile wet chemistry method", **Materials Research Bulletin**. 44(1): 146-150, 2009.

REFERENCES (CONTINUED)

[11] Zuoli He, et al. "Electrochemical behavior and photocatalytic performance of Nitrogen-doped TiO_2 nanotubes arrays powders prepared by combining anodization with solvothermal process", **Ceramics International**. 39: 5545-5552, 2013.

[12] T. Maiyalagan, B. Viswanathan, U. Varadaraju. "Fabrication and Characterization of uniform TiO_2 nanotube arrays by sol-gel template method", **Bulletin of Material Science**. 29(7): 705-708, 2006.

[13] J.M. Macak, H. Tsuchiya, P. Schmuki, "High-aspect-ratio TiO_2 nanotubes by anodization of titanium", **Angew. Chem. Int. Ed**. 44: 2100-2102, 2005.

[14] Hailei Li, et al. "Synthesis and investigation of TiO_2 nanotubes array prepared by anodization and their photocatalytic activity", **Ceramics International**. 38: 5791-5797, 2012.

[15] Buagan Samran, P. Kronkitsiri, et al. "Preparation and microstructure of titania nanotube arrays by anodization method", **Advanced Materials Research**. 802: 104-108, 2013.

[16] Hee Yeon Hwang, et al. "Influence of the organic electrolyte and anodization conditions on the preparation of well-aligned TiO_2 nanotube arrays in dye-sensitized solar cells", **Solar Energy**. 85: 1551-1559, 2011.

[17] Jiahua Ni, et al. "Preparation of near micrometer-sized TiO_2 nanotube arrays by high voltage anodization", **Materials Science and Engineering C**. 33: 259-264, 2013.

[18] Narongsak Kodtharin, Rinnatha Vongwatthaporn, Udom Tipparach. "The Phase Transformation and Structures of Titania Nanotubes Arrays prepared by Anodization Method", **UBRU International Conference**. 4: 455-459, 2014.

[19] Emmanuel Nyambod Timah, Buagun Samran, Udom Tipparach. "Fabrication and Characterization of TiO_2 nanotubes for Dye-Sensitized Solar Cells", **Journal of Material Science and Engineering**. 4: 61, 2015.

REFERENCES (CONTINUED)

[20] Nana Amponsah Kyerematеng, et al. "Properties of Sn-doped TiO_2 nanotubes fabricated by anodization of co-sputtered Ti-Sn thin films", **Electrochemical Acta**. 62: 192-198, 2012.

[21] Aadesh P. Singh, et al. "Iron doped nanostructured TiO_2 for photoelectrochemical generation of hydrogen", **International Journal of Hydrogen Energy**. 33: 5363-5368, 2008.

[22] Xiaobo Chen, et al. "Fabrication of 10 nm diameter TiO_2 nanotubes arrays by titanium anodization", **Thin Solid Films**. 515: 8511-8514, 2007.

[23] Hao Xu and et al. " Application of ultrasonic wave to clean the surface of the TiO_2 nanotubes prepared by the electrochemical anodization", **Applied Surface Science**. 257: 8478-8480, 2011.

[24] Wanichaya Mekprasat, Wisanu Pecharapa. "Synthesis and characterization of Nitrogen-doped TiO_2 photocatalytic activity enhancement under visible light", **Energy Procedia**. 9: 509-514, 2011.

[25] Zuoli He, et al. "Electrochemical behavior and photocatalytic performance of Nitrogen-doped TiO_2 nanotubes arrays powders prepared by combining anodization with solvothermal process", **Ceramics International**. 39: 5545-5552, 2013.

[26] Antonio Luque and Steven Hegedus (Editors). **Handbook of Photovoltaic Science and Engineering**. New York: John Wiley & Sons Ltd, 2003.

[27] Green M. **Solar Cells: Operating Principles, Technology and System Applications Chap. 1**. NJ: Prentice-Hall, Inc.,Englewood Cliffs, 1982.

[28] Brittany L., Oliva-Chatelain, Andrew R. Barron. (2011). "An Introduction to Solar Cell Technology", **An Introduction to Solar Cell Technology**. http://cnx.org/exports/dd0537a2-fb5d-439d-8feb-bf2e50656dae@1.pdf/an-introduction-to-solar-cell-technology-1.pdf. April, 2015.

[29] ETAP. (2015). "Photovoltaic Array Fundamentals", **Renewable Energy Software**. http://etap.com/renewable-energy/photovoltaic-101.htm?lang=en-US. May, 2015.

REFERENCES (CONTINUED)

[30] Green M., **Solar Cells: Operating Principles, Technology and System Applications Chap. 5**. NJ: Prentice-Hall, Inc.,Englewood Cliffs, 1982.

[31] P. K. Basu. **Theory of Optical Processes in Semiconductors – Bulk and microstructures**. UK: Clarendon Oxford University Press, 2003.

[32] John Singlenton, K. Seeger. "Electronic band structure", **Warwick–Department of Physics, Last Revision**. http://www2.warwick.ac.uk/fac/sci/physics. July, 2010.

[33] Xian-Wei Liu, Wen-Wei Li, Han-Qing Yu. "Cathodic catalytes in Bioelectrochemical systems for energy recovery from wastewater", **Chem. Soc. Rev**. 43: 7718-7745, 2014.

[34] Pierret R. **Semiconductor Device Fundamentals**. MA: Addison-Wesley, 1996.

[35] Pankove J. **Optical Processes in Semiconductors**. New York: Dover Publications, 1971.

[36] Felipe Valenz – Lecture Support Course 2 (pdf). (2012). "Electronic and Optical Properties of Nanomaterials", http://www.itp.epfl.ch/file/ AdvancedNanomatrials. May, 2015.

[37] Gabor L. Hornyak, et al. **Introduction to Nanoscience**. Florida: CRC Press – Taylor & Francis Group, 2008.

[38] Guozhong Cao. **Nanostructures & Nanomaterials – Synthesis, Properties & Applications**. US: Imperial College Press, 2004.

[39] Shannon . (2015). "TiO_2 Photocatalys", **PaveMaintenance**. https://pavemaintenance.wikispaces.com/TiO2+Photocatalys+-+Shannon. April, 2015.

[40] AZO Materials. (2015). "Titanium dioxide – titania (TiO_2) properties", **Titanium Dioxide - Titania (TiO2)**. http://www.azom.com/properties.aspx?ArticleID=1179. May, 2015.

[41] Diebold U. "The Surface Science of Titanium dioxide", **Surface Science. Rep**. 48: 53-229, 2003.

REFERENCES (CONTINUED)

[42] Wikipedia. (2009). “Titanium_dioxide”, **Titanium_dioxide**. https://en.wikipedia.org/wiki/Titanium_dioxide. July, 2015.

[43] Nowotny J., et al. “Titanium dioxide for Solar Hydrogen I. Functional properties”, **International Journal of Hydrogen Energy**. 32: 2609-2629, 2007.

[44] Agatino Di Paola, Marianna Bellarditaand Leonardo Palmisano. “Brookite, the Least Known TiO_2 Photocatalyst”, **Catalysts**. 3(1): 36-73, 2013.

[45] Charles Sorrell, Sunao Sugihara, Janusz Nowotny (editors), **Materials for energy conversion devices**. Cambridge: Woodhead Publishing Ltd, 2005.

[46] B.D. Cullity, S.R. Stock. **Elements of X-ray Diffraction**. 3rd ed. New Jersey: Prentice Hall, 2001.

[47] Charles W. Dunnill and Ivan P. Parkin, “Nitrogen-doped TiO_2 thin films: photocatalytic applications for healthcare environments”, **Dalton Trans**. 40: 1635-1640, 2011.

[48] Bing-Xin Lei, et al. “Fabrication of partially crystalline TiO_2 nanotube arrays using 1, 2-propanediol electrolytes and application in dye-sensitized solar cells”, **Advanced Powder Technology**. 24: 175-182, 2013.

[49] Hee Yeon Hwang, et al. “Influence of the organic electrolyte and anodization conditions on the preparation of well-aligned TiO_2 nanotube arrays in dye-sensitized solar cells”, **Solar Energy**. 85: 1551-1559, 2011.

[50] J.M. Macak, et al. “ Mechanistic aspects and growth of large diameter self-organized TiO_2 nanotubes”, **Journal of Electroanalytical Chemistry**. 621: 254-266, 2008.

[51] Yan Wang, et al. “Rapid anodic oxidation of highly ordered TiO_2 nanotube arrays”, **Journal of Alloys and Compounds**. 509: L157-L160, 2011.

[52] Jayant Dharma, Aniruddha Pisal, PerkinElmer. **Application note – UV/VIS/NIR Spectrometer**. New York: PerkinElmer Inc, 2009.

[53] Subhayan Biswas, et al. “Synthesis of thick TiO_2 nanotube arrays on transparent substrate by anodization technique”, **Electrochemistry Communications**. 12: 668-671, 2010.

REFERENCES (CONTINUED)

[54] Kathy Lu, Zhipeng Tian, Jeffrey A. Geldmeier. "Polishing effects on anodic titania nanotube formation", **Electrochemical Acta**. 56: 6014-6020, 2011.

[55] Srimala Sreekantan, et al. "Influence of electrolyte pH on TiO_2 nanotubes formation by Ti anodization", **Journal of Alloys and Compounds**. 485: 478-483, 2009.

[56] J.Y. Lin, et al. "Effects of rapid thermal annealing on the structural properties of TiO_2 nanotubes", **Applied Surface Science**. 258: 530-534, 2011.

[57] Jiahua Ni, et al. "Preparation of near micrometer-sized TiO_2 nanotube arrays by high voltage anodization", **Materials Science and Engineering C**. 33: 259-264, 2013.

[58] Hao Wen, et al. "Synthesis and electrochemical properties of CeO_2 nanoparticle modified TiO_2 nanotube arrays", **Electrochemical Acta**. 56: 2914-2918, 2011.

[59] Sebastian Bauer, et al. "Size-effects in TiO_2 nanotubes: Diameter dependent anatase/rutile stabilization", **Electrochemistry Communications**. 13: 538-541, 2011.

[60] Rui Liu, et al. "Applying the statistical experimental method to evaluate the process conditions of TiO_2 nanotube arrays by anodization method", **Current Applied Physics**. 11: 1294-1298, 2011.

[61] Rui Liu, et al. "Fabrication of TiO_2 nanotube arrays by electrochemical anodization in an NH_4F/H_3PO_4 electrolyte", **Thin Solid Films**. 519: 6459-6466, 2011.

[62] S. Zhou, et al. "Preparation and photocatalytic properties of N-doped nano-TiO_2/muscovite composite", **Applied Surface Science**. 258: 6136-6141, 2012.

[63] H. Irie, Y. Watanabe, K. Hashimoto. "Nitrogen-concentration dependence on photocatalytic activity of TiO_2 nanotube powers", **Journal of Physics and Chemistry B**. 107: 5483-5486, 2003.

REFERENCES (CONTINUED)

[64] N.T. Nolan, et al. "Effect of N-doping on the photocatalytic activity of sol-gel TiO_2", **Journal of Hazardous Materials**. 211(212): 88-94; April, 2011.

[65] He Z.L., et al. "photocatalytic degradation of methyl orange over nitrogen-fluorine codoped TiO_2 nanobelts prepared by solvothermal synthesis", **ACS Applied materials & Interfaces**. 4: 6816-6826, 2012.

[66] T. Kubo, A. Nakahira. "Local Structure of TiO2-Derived Nanotubes Prepared by the Hydrothermal Process", **J Phys Chem C**. 112(5): 1658-1662, 2008.

[67] H.M. Yates, et al. " The role of nitrogen doping on the development of visible light-induced photocatalytic activity in thin TiO_2 films grown on glass by chemical vapor deposition", **J. Photochem. Photobiol**. 179: 213-223, 2006.

[68] Soon Hyung Kang, et al. "Synthesis of nanobranch TiO_2 nanotubes and their application to dye-sensitized solar cells", **Current Applied Physics**. 13: 252-255, 2013.

[69] Kiyoung Lee, Patrik Schmuki. "Ta doping for an enhanced efficiency of TiO_2 nanotube based dye-sensitized solar cells", **Electrochemistry Communications**. 25: 11-14, 2012.

[70] Xiang Li, Rongchun Xiong, Gang Wei. "Preparation of photocatalytic activity of nanoglued Sn-doped TiO_2", **Journal of Hazardous Materials**. 164: 587-591, 2009.

[71] Ho Chang, et al. "Photoelectrode thin film of dye-sensitized solar cells fabricated by anodizing method and spin coating and electrochemical impedance properties of DSSC", **Applied Surface Science**. 275: 252-257, 2013.

[72] Hun Park, et al. "Fabrication of dye-sensitized solar cells by transplanting highly ordered TiO_2 nanotube arrays", **Solar Energy Materials & Solar Cells** 95: 184-189, 2011.

[73] Yongping Fu, et al. "Dye-sensitized solar cell tube", **Solar Energy Materials & Solar Cells**. 102: 212-219, 2012.

REFERENCES (CONTINUED)

[74] Yandong Duan, et al. "Influence of Sn source on the performance of dye-sensitized solar cells based on Sn-doped TiO_2 photoanodes: A strategy for choosing an appropriate doping source", **Electrochemical Acta**. 107: 473-480, 2013.

[75] Hua Tian, et al. " Hydrothermal synthesis of S-doped TiO_2 nanoparticles and their photocatalytic ability for degradation of methyl orange", **Ceramic International**. 35: 1289-1292, 2009.

[76] B. Samran, et al. "Fabrication and Characterization Anodized Titania nanotubes for Enhancing Hydrogen Generation", in **The 8th Annual Conference of Thai Physics Society**. P.255-258. Chiang Mai: Chiangmai Grandview Hotel, 2013.

[77] Poulomi Roy, Sergiu P. Albu, Patrik Schmuki. "TiO_2 nanotube in dye-sensitized solar cells: Higher efficiencies by well-defined tube tops", **Electrochemistry Communications**. 12: 949-951, 2010.

[78] Ning Liu, Kiyoung Lee, Patrik Schmuki. "Small diameter TiO_2 nanotubes vs. nanopores in dye-sensitized solar cells", **Electrochemistry Communications**. 15: 1-4, 2012.

[79] Y.L. Cheong, et al. "Room-temperature synthesis of nanocrystalline titanium dioxide via electrochemical anodization", **Materials Science in Semiconducting Processing**. 26: 130-136, 2014.

[80] Shih-Yu Ho, et al. "Fabrication of TiO_2 nanotube-nanocube array composite electrode for dye-sensitized solar cells", **Thin Solid Films**. 529: 123-127, 2012.

[81] Kang-Pil Kim, et al. "Dye-sensitized solar cells based on trench structured TiO_2 nanotubes in Ti substrate", **Current Applied Physics**. 13(4): 795-798, 2013.

[82] Etsushi Tsuji, et al. "Preparation of non-annealed anatase TiO_2 film on ITO substrate by anodizing in hot phosphate/glycerol electrolyte for dye-sensitized solar cells", **Materials Letters**. 91: 39-41, 2013.

REFERENCES (CONTINUED)

[83] Emmanuel Nyambod Timah, et al. “Photocatalytic Performance of Fe-doped TiO_2 nanotubes for DSSCs”, in **Southeast Asia Conference on Thermoelectric C4O02**. P. 91-92. Champasak: Champasak Grand Hotel, 2014.

[84] Bao Yuan, et al. “Nitrogen doped TiO_2 nanotube arrays with high photoelectrochemical activity for photocatalytic applications”, **Applied Surface Science**. 280: 523-529, 2013.

[85] Ming Li, et al. “Synthesis of TiO_2 submicro-rings and their application in dye-sensitized solar cell”, **Applied Energy**. 88: 825-830, 2011.

[86] Liangliang Yin, et al. “Understanding the growth behavior of titania nanotubes”, **Electrochemistry Communications**. 13: 454-457, 2011.

CURRICULUM VITAE

NAME	Emmanuel Nyambod Timah
NATIONALITY	Cameroonian
BIRTH DATE/PLACE	26-12-1978 at Mankon Mezam, North West, Cameroon
EMAIL/CELL	timahe@yahoo.com ; 081 052 5337
EDUCATION	2001 DIPES 1 Secondary/High School Teaching Diploma [ENS Bambili, University of Yaounde 1, Cameroon] 2003 BSc Physics [University of Yaounde 1, Cameroon] 2004 MSc Physics [University of Yaounde 1, Cameroon] 2006 DEA Physics[University of Yaounde 1, Cameroon]
PROCEEDINGS & PUBLICATIONS	1. Emmanuel Nyambod Timah, Rinnatha Vongwantthaporn, Narongsak Kodtharin and Udom Tipparach, "Photocatalytic Performance of Fe-doped TiO_2 nanotubes for DSSCs". Proceedings of SACT 2014 # C4O02; (Accepted June 2015 for Journal of Materials Science and Applied Energy) 2. Emmanuel Nyambod Timah, Buagan Samran and Udom Tipparach, "Fabrication and Characterization of TiO_2 nanotubes for Dye-Sensitized Solar Cells". Accepted Proceedings NanoThailand Vol 4: No. 61, 2014 [Accepted July 2015 for publication in Journal of Material Science and Engineering]
TEACHING CAREER PROFILE	2013-2015 Princess Chulaborn's College Mukdahan, Thailand 2010-2013 Srinagarindra the Princess Mother School Sisaket, Thailand 2009-2010 Saigon International College, Ho Chi Minh, Vietnam 2007-2008 Saard Phaderm Wittaya School Chumphon, Thailand

CURRICULUM VITAE (CONTINUED)

2006-2007 Anuban Sisaket School, Sisaket, Thailand

2004-2006 Unity Bilingual School, Yaounde, Cameroon

OTHERS Co-Editor, “Discovery Science” Author: Dr. Udom Tipparach Publisher: Pada Education Co. Ltd, 2014